Journal of Energy Storage 107 (2025) 114934

Contents lists available at ScienceDirect

Journal of Energy Storage

journal homepage: www.elsevier.com/locate/est

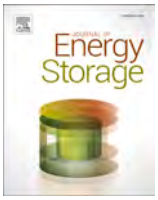

Research papers

High-performance nickel-zinc battery composed of SiC-coated zinc anode and MoCoCu-P coated nickel foam cathode

Caijin Yang [a,1], Xue Wang [a,1], Dajun Wu [b,*], Fanya Jin [c], Zhenzhong Yang [a], Shaohui Xu [a,d,**], Dayuan Xiong [a], Lianwei Wang [a], Paul K. Chu [d]

[a] Key Laboratory of Polar Materials and Devices, Ministry of Education, and School of Physics and Electronic Science, East China Normal University, 500 Dongchuan Road, Minhang District, Shanghai 200241, China
[b] Jiangsu Laboratory of Advanced Functional Materials, School of Electronic and Information Engineering, Changshu Institute of Technology, Changshu 215500, China
[c] Southwest Institute of Physics of Nuclear Industry, Chengdu 610041, China
[d] Department of Physics, Department of Materials Science & Engineering, and Department of Biomedical Engineering, City University of Hong Kong, Tat Chee Avenue, Kowloon, Hong Kong, China

ARTICLE INFO

Keywords:
Ni-Zn battery
SiC
Medium-entropy alloy
Synergistic effects

ABSTRACT

A high-performance nickel-zinc alkaline battery comprising a SiC-coated Zn anode and MoCoCu-P medium-entropy alloy-coated nickel foam cathode is designed and fabricated. The battery shows a large areal capacity 4.0 mAh cm^{-2} (15.0 mA cm^{-2}), and excellent cyclability for 45 h (areal capacity 1.5 mAh cm^{-2} at 60.0 mA cm^{-2}). The energy density and power density are 6.25 (4.41) mWh cm^{-2} and 31.1 (60.2) mW cm^{-2}, respectively, at a current density of 15 (40) mA cm^{-2}. The outstanding properties of the Ni-Zn alkaline battery stem from the improved Zn plating/stripping process through SiC coating on Zn anode, synergistic effects rendered by the different ingredients, as well as the hybrid redox process of Ni and Cu for medium-entropy alloy-coated nickel foam cathode.

1. Introduction

Zn-based energy storage devices are promising due to the more abundant natural reserve, lower cost, safety, as well as higher volumetric capacity (5854 Ah l^{-1}) and gravimetric capacity (820 mAh g^{-1}) compared to Li-ion batteries [1–3]. In particular, nickel-zinc (Ni-Zn) batteries are attractive on account of the high theoretical specific energy (372 Wh Kg^{-1}) and deeper discharge depth of Zn (>40 %). Even at a small Zn discharge depth of ~20 %, Ni-Zn batteries are comparable or superior to lead-acid and nickel-cadmium batteries [4]. Hence, efforts have been made to develop multifarious Ni-Zn batteries [5–7]. However, the electrochemical properties of Ni-Zn batteries are still not satisfactory because of the small practical specific energy, poor Coulombic efficiency, and propensity for dendritic failure.

In the anodic oxidation process for Ni-Zn secondary alkaline system, Zn loses two electrons and is dissolved into the electrolyte during discharging, while Zn metal is formed by reduction on the anode during charging. However, Zn tends to form a rough and nonuniform electrodeposit due to losses of active materials, and the dendritic structure can lead to a short circuit [6–8]. In order to improve the stability in an alkaline electrolyte, surface engineering has been proposed to mitigate the side reactions and dendrite suppression [9–16]. With the help of Triethanolamine, modified binder Zn anode shows the leveling effect and good electrochemical reversibility and offers a promising method to build Ni-Zn battery with longer cycling life and superior energy efficiency [9]. By using zincophilic Sn nanoparticles and N-doped carbon to control the homogeneous Zn deposition, dendrite formation can be reduced, leading to high Coulombic efficiency, low voltage hysteresis, and better cycling stability [11]. A nonstoichiometric silicon nitride (SiN_x) film with specific defects can modify the surface properties to enhance the stability of Zn anodes. The Si dangling bonds Si DBs and zincophilic N sites enable uniform distribution of Zn^{2+} on the anode for even Zn deposition. As a result, the SiN_x@Zn symmetrical battery shows a long lifespan of >4600 h at 1 mA cm^{-2} [13]. The surface protective

* Corresponding author.
** Corresponding author at: Key Laboratory of Polar Materials and Devices, Ministry of Education, and School of Physics and Electronic Science, East China Normal University, 500 Dongchuan Road, Minhang District, Shanghai 200241, China.
E-mail addresses: 201700028@cslg.edu.cn (D. Wu), shxu@ee.ecnu.edu.cn (S. Xu).
[1] These authors contributed to the work equally and should be regarded as co-first authors.

https://doi.org/10.1016/j.est.2024.114934
Received 27 September 2024; Received in revised form 28 November 2024; Accepted 2 December 2024

layer would be a suitable method to inhibit Zn dendrite formation through minimizing direct contact with the electrolyte and affect the diffusion behavior of Zn^{2+} ions and free water molecules.

The conversion process on the cathode of the Ni-Zn battery exploits the redox transition of the metals between oxide and hydroxide or oxyhydroxide, such as the Ni^{2+}/Ni^{3+} redox couples and Faradaic reactions between $Ni(OH)_2$ and NiOOH [17–19]. However, similar to other electrode materials, these cathodes suffer from repeated lattice expansion/ contraction and strain generated from H^+ insertion/extraction during charging/discharging, resulting in structure failure and poor cyclic stability. Hence, the practical application of Ni-Zn batteries has been plagued by the restrictive capacity density and degradation of the Ni-based cathode. Cathode materials with both high capacity and cycling characteristics are challenging due to the high polarization of bivalence. For Ni-based ionic compounds, Ni_3S_2 and $Ni_{12}P_5$ have been proposed for the Ni-Zn battery cathode, but the low capacity limits the energy density [20–22]. The rapid capacity decay during charging/discharging cycles arises from the large volume change and generation of cracks that collapse the original morphology and structure [18]. Therefore, a structurally robust Ni cathode is required to achieve a high energy density and long cycle lifetime. Recently, Medium-entropy alloys (MEAs) have attracted more attentions due to their superior mechanical performance, unusual thermal and electronic transport properties, and anticorrosion [23–26]. MEAs are composed of mixtures of equal or relatively large proportions of three or four primary elements. Which have a less complex structure, making the identification of active sites more convenient. Also, strategies to control the functional atoms and the specific atomic configuration in the MEAs would best promote the electrochemical reaction. Due to the excellent mechanical and electrical properties, MEAs are used to modulate the electrode properties and improving the performance of energy devices, including of water electrolysis, Li ion battery and Zn-air battery [27–30].

In order to improve the properties of the Ni-Zn battery, anode and cathode should totally be improved through modulation the surface properties. Furthermore, it is necessary to understand the electrochemical processes at the anode and cathode of Ni-Zn battery. In this work, SiC is deposited by magnetron sputtering on the Zn foil to improve the stability of the Zn anode. Moreover, electrodeposition of the MoCoCu-P medium-entropy alloy is performed to coat the nickel foam (NF) to improve the capacity of the Ni-Zn battery. The full-cell Ni-Zn battery composed of the SiC-Zn anode and MoCoCu-P/NF cathode shows a large areal capacity, high energy (power) density, and excellent cyclability.

2. Experimental details

2.1. Electrode synthesis

The SiC coatings were deposited onto the polished Zn foil (99.9 % pure with a thickness of 0.2 mm) by reactive magnetron sputtering in mixed N_2-Ar (99.99 % purity for each gas). During deposition, the working pressure was kept at 3.5 Pa, and the total gas flow was maintained at 60 sccm. The DC power of the SiC target was 250 W with the suitable deposition time (10 min.). Annealing was performed at 300 °C under N_2 after deposition (sample designated as SiC-Zn). For comparison, the oxidic acid polished Zn (OA-Zn) was also prepared [31].

The alkaline gel solid-state electrolyte was prepared through dropping 7 mL acrylic acid in 7 mL deionized (DI) water, and adding the NaOH solution (4 g sodium hydroxide in 7 mL DI water), and stirring in an ice bath (10 min). Later, 110 mg of ammonium persulfate (initiator) and 4.2 mL of N-N′- dimethyl acrylamide (crosslinker) were added slowly and stirred (30 min). Afterward, the electrolyte was poured into a mold and dried at 70 °C for 1 h to form a transparent and flexible hydrogel film. Last, the film was peeled off and immersed in a solution composing of 5 mol L^{-1} potassium hydroxide (NaOH) and 0.1 mol L^{-1} $Zn(CH_3COO)_2 \cdot 2H_2O$ for 12 h.

A medium-entropy alloy MoCoCu-P layer was coated on the nickel foam (NF) by electrodeposition. 4.2 mmol $NaH_2PO_2{\cdot}H_2O$, 3.8 mmol $(NH_4)_2SO_4$, 6 mmol $CuSO_4{\cdot}5H_2O$, 6 mmol $CoSO4{\cdot}7H_2O$, 3 mmol Na_2MoO_4 were dissolved in 50 mL DI water. $(NH_4)_2SO_4$ was the buffering agent for the pH and prevented oxidation during electroplating [28]. The electrodeposition was performed using a three-electrode configuration at room temperature on the electrochemical workstation VMP3 (Bio-Logic). Pt foil (NF) was the counter (working) electrode, and saturated calomel electrode (SEC) was the reference electrode. After electrodeposition at the different potentials from −1.0 to −2.5 V vs. SCE during the time 40 min, the samples were thoroughly washed with deionized water and then dried for 6 h at 40 °C to obtain the MoCoCu-P coated NF electrode (marked as MoCoCu-P/NF-n, with n representing the electrodeposition potential). All the chemicals and reagents were analytical grade and used without purification. The aqueous solutions were prepared with deionized (DI) water (18.2 MΩ cm).

2.2. Materials characterization

The crystal structures were determined on the X-ray diffractometer (XRD) with Cu K_α radiation (k = 1.5406 Å). The morphology and composition of the samples were characterized by field-emission scanning electron microscopy (FE-SEM, Hitachi S-4800, Japan), and the surface chemical compositions were determined by X-ray photoelectron spectroscopy (XPS) with Al K_α irradiation. Transmission electron microscopy (TEM) was conducted to examine the fine structure, and Raman scattering was performed to analyze the vibrational modes using a 514 nm laser. The specific surface area and pore size distributions were determined on the Micromeritics ASAP 2020 N_2 adsorption analyzer.

2.3. Electrochemical evaluation

The electrochemical measurements were performed using a three-electrode configuration on the VMP3 (Bio-Logic) in 1.0 mol L^{-1} KOH solution (pH = 13.6). The MEA-coated nickel foam was the working electrode, Pt foil was the counter electrode, and SCE was the reference electrode. Cyclic voltammetry (CV) was carried out at different scanning rates. The electrochemical impedance spectra (EIS) were acquired at the open-circuit potential (OCP) in the frequency range of 0.1 Hz to 100 kHz. The two-electrode configuration was also used to analysis of the battery. Galvanostatic charging-discharging was carried out at different current densities with the reference potential Zn/Zn^{2+} on the Land system (Wuhan Land, China). All the measurements were performed at room temperature (25 °C), and the results were normalized by the footprint area.

3. Results and discussion

Three steps were designed to understand the properties of anode and cathode in Ni-Zn batteries. First step, the properties of SiC-Zn anodes were discussed based on Ni-Zn batteries composed of SiC-Zn anode and NF cathode sandwiching the alkaline gel solid-state electrolyte (marked as SiC-Zn||NF, Section 3.1). Second step, the properties of MoCoCu-P coated NF cathodes were discussed based on Ni-Zn batteries composed of Zn anode and MoCoCu-P/NF cathode sandwiching the alkaline gel solid-state electrolyte (marked as Zn||MoCoCu-P/NF, Section 3.2). Last step, Ni-Zn batteries composed of SiC-Zn anode and MoCoCu-P/NF cathode were fabricated, as shown the Schematic in Fig. 1a (marked as SiC-Zn||MoCoCu-P/NF, Section 3.3). Photograph of flexible Ni-Zn battery was shown in Supplementary Fig. S1.

3.1. SiC-coated Zn anode (SiC-Zn)

Fig. 1b presents the typical XRD pattern of the SiC-coated Zn sample. The main XRD peaks at 36.54°, 39.30°, 43.52.0°, 54.62°, 70.34°, 70.88°, 83.82°, 83.82°, and 86.74° are associated with the (002), (10), (101),

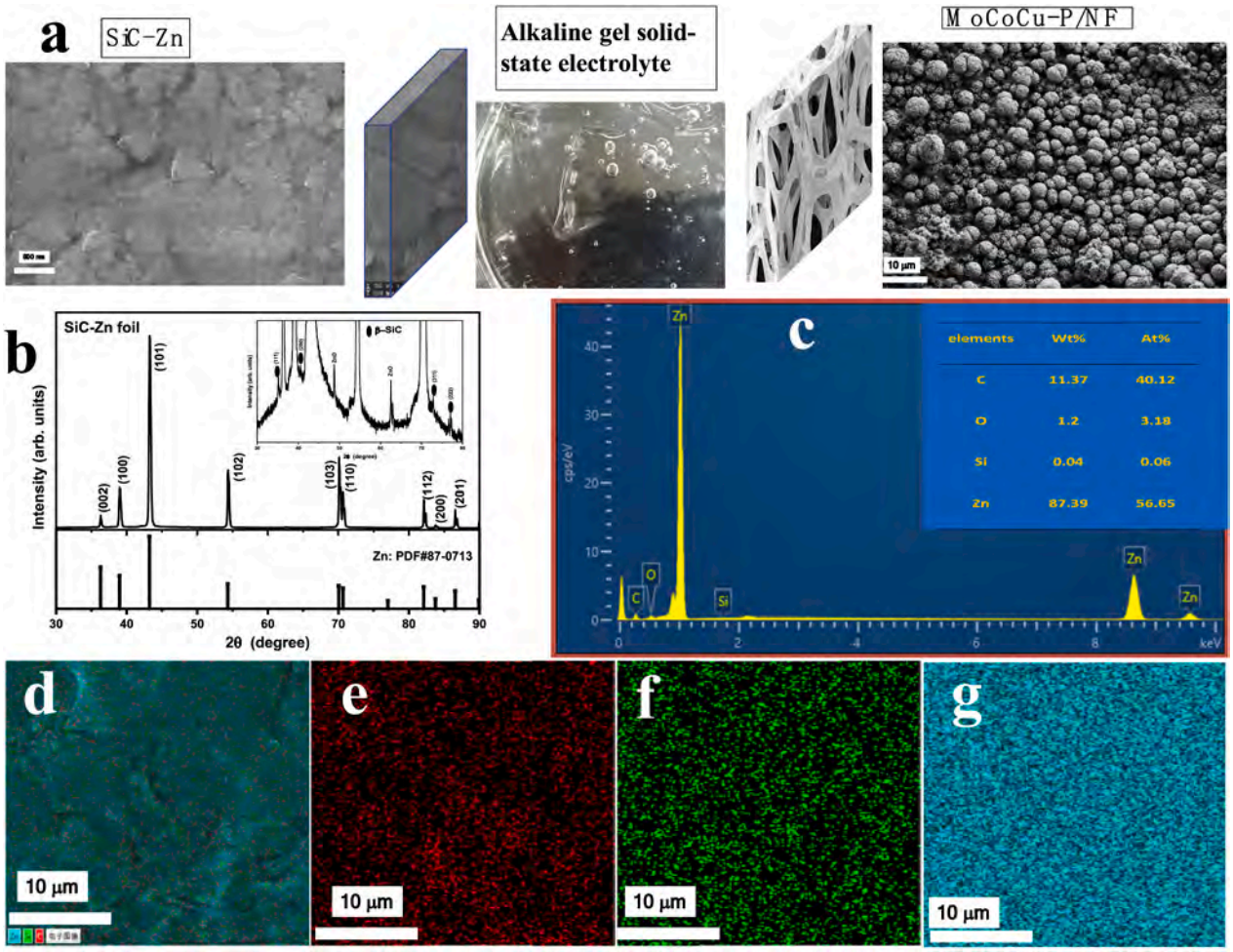

Fig. 1. (a) Schematic of the Ni-Zn battery composed of the SiC-Zn anode, alkaline gel solid-state electrolyte, and MoCoCu-P-coated nickel foam (NF) cathode. Structural characterization of the SiC-Zn electrode: (b) XRD, (c) EDS, and EDS elemental maps of (e) C, (f) Si, (g) Zn, and (d) All elements.

(102), (103), (110), (112), (200), and (201) planes of the closely packed hexagonal structure of Zn (JCPDS No. 87-0713) [14]. The peaks at 35.14°, 40.58°, 72.80°, and 77.04° are associated with the (111), (200), (311), and (222) planes of the cubic 3C-SiC structure (JCPDS No.29-1129, inset in Fig. 1b) arising from the deposited SiC layer [32]. There is less ZnO shown by the weak XRD peaks at 48.74° and 62.52° [33]. The morphology and microstructure of the product are examined by scanning electron microscopy (SEM). The surface morphology does not change after SiC deposition (Supplementary Fig. S2), and it only covers a part of the Zn surface (Fig. 1a). C and Si elements are detected by EDS, but the amount of deposited SiC is small (Fig. 1c). The Si concentration can be used to estimate SiC deposition (0.06 at.%). The elemental maps reveal a uniform distribution of Zn (Fig. 1g) together with small amounts of uniformly distributed C and Si (Fig. 1e–f). Only a part of the Zn surface is covered by the SiC layer, as shown in Fig. 1d.

To assess the effects of the SiC coating, the Ni-Zn battery composed of the SiC-Zn anode and NF cathode is fabricated (SiC-Zn||NF), and the charging-discharging curves at a current density of 5 mA cm^{-2} are shown in Fig. 2a, which also shows the curves of Zn||NF and OA-Zn||NF batteries for comparison. All the curves show the typical galvanostatic voltage profiles with the discharge voltage platforms between 1.80 and 1.6 V [34]. The Coulombic efficiency of the SiC-Zn||NF battery is 87.3 %, which is higher than those of the OA-Zn||NF (65.4 %) and Zn||NF (51.0 %) batteries. The discharge areal capacity decreases from 0.058 to 0.031 mAh cm^{-2} with increasing discharge current densities from 5 to 40 mA cm^{-2} for the SiC-Zn||NF battery (Fig. 2b). The Coulombic efficiency is higher at a larger current density. It increases to 95.4 %, 98.04 %, and 98.11 % at current densities of 10, 20, and 40 mA cm^{-2}. A similar trend is observed from the OA-Zn||NF and Zn||NF batteries (Supplementary Fig. S3). In order to show clearly, the charge (discharge) areal capacities and the Coulombic efficiencies versus the current densities are shown in Fig. 2c. The high Coulombic efficiency of the SiC-Zn||NF battery can be attributed to the efficient Zn plating/striping process, which introduces overlapping of the charge and discharge areal capacities at different current densities. Owing to the low striping Zn process (large charge capacity), low Coulombic efficiency is observed from the Zn||NF battery even at a high discharge capacity. The low discharge capacity also limits the Coulombic efficiency of OA-Zn||NF battery. The discharge areal capacities versus cycle number are shown in Fig. 2d for different Ni-Zn batteries. The coating process improves the cycling stability of Ni-Zn batteries, as manifested by 1200 cycles for the OA-Zn||NF and SiC-Zn||NF batteries. The areal capacity decreases from 0.07 (0.058) to 0.058 (0.038) mAh cm^{-2} for the SiC-Zn||NF (OA-Zn||NF) battery. The cycle number only reaches about 700 for the Zn||NF battery, and even a "soft short" is shown at about 200 cycles [35].

In order to understand the high stability of the SiC-Zn||NF battery, electrochemical tests are done on the full cell, as shown in Fig. 3. Cyclic voltammetry (CV) curves reveal high oxidation/reduction current peaks for the Zn potential region (Fig. 3a, potentials from −0.5 to 0.5 V vs. Zn/Zn^{2+}). The cathode (anode) current density of the SiC-Zn||NF battery is about −150 (23.4) mA cm^{-2}, which is higher than those of Zn||NF and OA-Zn||NF. The electrochemical process on the cathode is influenced by the surface coating on the Zn anode. As shown the CV curves in Fig. 3b, the Ni region (1.0 to 2.2 V vs. Zn/Zn^{2+}) shows a high oxidation peak for

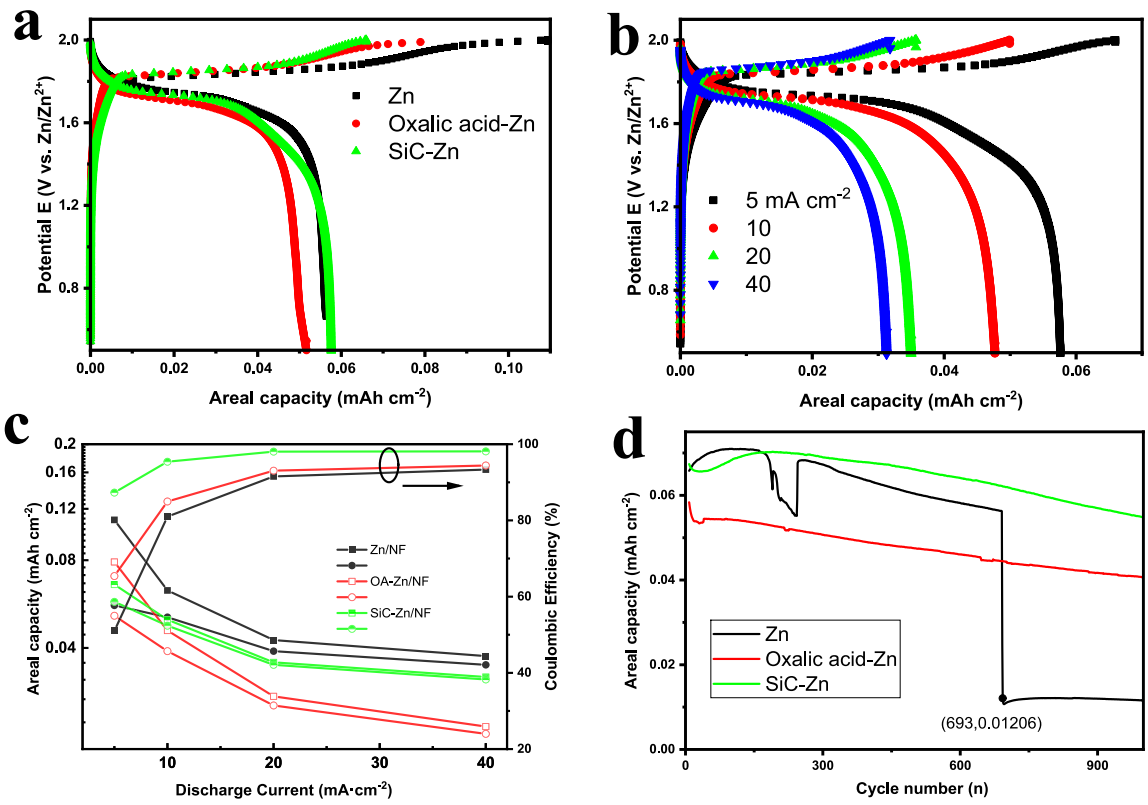

Fig. 2. Properties of Ni-Zn batteries composed of the SiC-Zn anode and NF cathode (SiC-Zn||NF). (a) Charging-discharging curves at a current density of 5 mA cm^{-2}, (b) Charging-discharging curves of the SiC-Zn||NF battery at different current densities from 5 to 40 mA cm^{-2}, (c) Areal capacity and efficiency versus current density, and (d) Cycling stability.

the NF cathode after SiC deposition. The current density of the oxidation peak of SiC-Zn||NF battery is 52.53 mA cm^{-2} at potential 1.967 V vs. Zn/Zn^{2+}, which is larger than those of OA-Zn||NF (30 mA cm^{-2}) and Zn||NF (27 mA cm^{-2}). The reduction current density and reversion potential (34.04 mA cm^{-2} at 1.71 V vs. Zn/Zn^{2+}) of the SiC-Zn||NF battery are higher than those of OA-Zn||NF (27.6 mA cm^{-2} at 1.68 V vs. Zn/Zn^{2+}) and Zn||NF (21.9 mA cm^{-2} at 1.69 V vs. Zn/Zn^{2+}).

In order to analyze the electrochemical process on the cathode, CV curves are acquired from the SiC-Zn||NF battery at different sweeping rates, as shown in Fig. 3c. The CV curves of OA-Zn||NF and Zn||NF are shown in Supplementary Fig. S4. With increasing sweeping rates from 10 to 70 mA cm^{-2}, positive shift is observed from 1.937 to 2.02 V vs. Zn/Zn^{2+} for oxidation peaks, and the current density increases from 13.4 to 36.56 mA cm^{-2}. However, the reduction peaks shift to a low potential with increasing current densities at low scanning rates from 10 to 40 mV s^{-1}, after which the current density remains constant at 22 mA cm^{-2}, and the peaks shift to low potential at high scanning rates between 40 and 70 mV s^{-1}. The current densities of the oxidation and reduction peaks versus scanning rates are shown in the inset Fig. 3c. Compared to the Zn||NF battery, an improved Ni redox process corresponding to large current densities of the oxidation and reduction peaks is observed for SiC-Zn. The slope of 0.576 of the oxidation peaks versus sweep rates is larger than that of the Zn||NF battery (slope of 0.495) [36]. However, the reduction process on the NF cathode is limited at high sweep rates (or high current densities). The plating process is monitored by optical microscopy after the battery test (Supplementary Fig. S5). SiC deposition smooths the Zn surface, and the SiC thickness is <100 nm. After the Ni-Zn battery test, Zn dendrites emerge from the pristine Zn surface but a smooth surface is observed from the SiC-coated Zn anode, although the similar XRD patterns are shown including of the Zn and ZnO peaks (Supplementary Fig. S6).

Electrochemical impedance spectroscopy is performed at the open-circuit potential (OCP) for the full cell, as shown in Fig. 3d (Nyquist plot). The semicircle in the high-frequency region indicates the charge transfer resistance (R_1), and the line in the low-frequency region corresponds to the semi-infinite Warburg impedance because of the diffusion-limited electron transfer process [37,38]. According to fittings (equivalent electrical circuit and fitting results are shown in inset Fig. 3d), the SiC-Zn||NF battery shows an extremely small shunt resistance R_S (0.51 Ω cm^2) and charge transfer resistance R_1 (3.88 Ω cm^2), verifying the good electrical conductivity and fast surface redox process [38]. The excellent electrochemical properties of the SiC-Zn||NF battery can be ascribed to thin SiC layer, sufficient interfacial contact with the electrolyte, and more ion channels, which shorten the ion diffusion pathway and facilitate fast electron transport.

3.2. *MoCoCu-P coated nickel foam cathode (MoCoCu-P/NF)*

The MoCoCu-P MEA is electrodeposited on NF at different potentials from −1.0 V to −2.5 V vs. SCE during time 40 min (MoCoCu-P/NF-n, where n represents the deposition voltage) [28]. The load would be 0.0197 g cm^{-2} at the potential −2.0 V vs. SCE as listed in Supplementary Table S1. SEM reveals an irregular dendritic layer composed of nanoparticles at deposition potential −1.0 V vs. SCE (MoCoCu-P/NF-1, Supplementary Fig. S7a–c). At deposition potential −2.0 V vs. SCE, NF is coated with uniform particles (1–3 μm) (MoCoCu-P/NF-2, Supplementary Fig. S7d–f). At deposition potential −2.5 V vs. SCE, an irregular dendritic layer is observed (MoCoCu-P/NF-2.5, Supplementary Fig. S7h–j). Hence, surface morphology is sensitive to the deposition potential, and a moderate potential such as −2.0 V vs. SCE produces a uniform coating.

Fig. 4a shows the XRD spectrum of MoCoCu-P/NF-2, and the peaks at 44.42°, 51.81°, and 76.31° correspond to the (111), (200), and (220) planes of NF (PDF#04-0850) [39]. The weak XRD peak at 43.29° arises

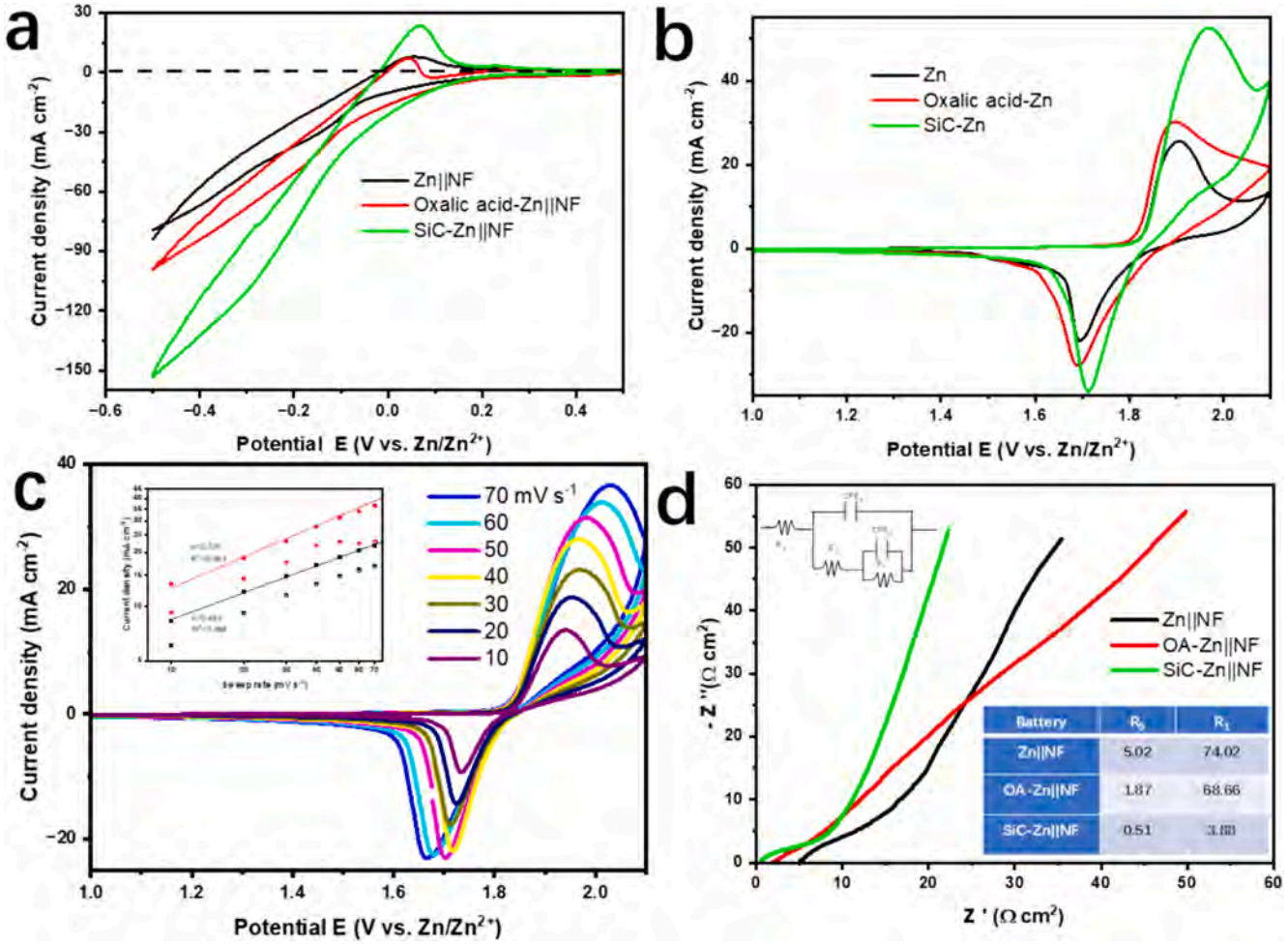

Fig. 3. Electrochemical properties of Ni-Zn batteries comprising the SiC-Zn anode and NF cathode. Cyclic voltammetry (CV) curves: (a) Zn anode potential region and (b) Ni cathode potential region; (c) CV curves at different sweeping rates in the Ni cathode potential region with the inset showing the current density versus scanning rates for the anodic and cathodic peaks; (d) Electrochemical impedance spectra (EIS) with the inset showing the equivalent circuit and fitting data.

from the (111) plane of the face-centered cubic (FCC) CoCu phase (PDF# 50-1452) [40], in which Co and Cu constitute the matrix, whereas Mo and P are dopants. The N_2 adsorption-desorption isotherm curves of MoCoCu-P/NF-2 in Fig. 4b show that the MEA has a specific surface area of 17.55 m^2 g^{-1}. According to the Barrett-Joyner-Halena adsorption model, the pore size is 2.5 to 5 nm, indicating mesoporous and microporous characteristics. Catalysts with more micropores have more active sites and better contact between the active sites and substrate [40].

MoCoCu-P/NF-2 is examined by transmission electron microscopy (TEM) and high-resolution TEM (HR-TEM, Fig. 4c and d). It has a nanorod structure covered by nanosheets with a diameter of 10 nm and length of 100 nm (Fig. 4c). Fig. 4d shows short-range lattice fringes for a disordered structure and shows that MoCoCu-P/NF-2 has a lattice spacing of about 1.04 nm corresponding to 5-period (111) plane of CuCo (0.21 nm) [41]. Fig. 4f–j shows Co, Ni, Cu, Mo, and P, and Fig. 4e shows uniform distributions in the MEA nanoparticles with no apparent segregation. The Co and Cu concentrations are large, and there are fewer Mo and P. These results corroborate that the CuCo alloy is the matrix, as shown in XRD data. Supplementary Fig. S8 indicates that MoCoCu-P/NF-2 primarily comprises Mo, Co, Cu, and P together with O. XPS shows that the atomic concentrations of Mo, Co, Cu, and P are 15.81 %, 35.30 %, 36.2 %, and 12.69 %, respectively. Based on atomic concentrations of different elements, the structure entropy can be calculated 1.228 R, which belongs to the medium-entropy alloy (from 1R to 1.5 R) [42].

The charging-discharging curves in Supplementary Fig. S9a are acquired from the three-electrode system in the potential region 0.4 to −0.5 V vs. SCE. The maximum areal capacity of MoCoCu-P/NF-2 is 1.05 mAh cm^{-2} at 15 mA cm^{-2}. High areal capacities (from 1.1 to 0.85 mAh cm^{-2}) and Coulombic efficiency (~95 %) are shown for 600 cycles at a current density of 60 mA cm^{-2} (Supplementary Fig. S9b). Fig. 5a presents the charging-discharging of the Ni-Zn full cell with the MEA-coated NF cathode at a current density of 30 mA cm^{-2} in the voltage region from 2.0 to 0.5 V vs. Zn/Zn^{2+}. In the full cell composed of the MoCoCu-P/NF-2 cathode, the sloping voltage plateau extends from 1.9 V to 1.25 V, reaching a high areal capacity of 1.72 mAh cm^{-2}. Low areal capacities (0.22 and 0.44 mAh cm^{-2}) are observed from the full cell composed of the MoCoCu-P/NF cathode deposited at positive potentials (−1.0 and −1.5 V vs. SCE). The low areal capacity of 0.5 mAh cm^{-2} is also observed from the full cell consisting of the MoCoCu-P/NF cathode deposited at the negative potential (−2.5 V vs. SCE). The charging-discharging profiles of MoCoCu-P/NF-1 and MoCoCu-P/NF-2 for different current densities are shown in Fig. 5b–c. As the current density goes up from 15 to 100 mA cm^{-2}, the areal capacity decreases from 0.39 to 0.14 mAh cm^{-2} for the former and from 2.0 to 0.75 mAh cm^{-2} for the latter.

Fig. 5d shows the areal capacities versus current densities of the Ni-Zn full cells with different MEA cathodes. Excellent rate capability is observed from the Ni-Zn full cell with the MoCoCu-P/NF-2 cathode. The areal capacity is 2.0 mAh cm^{-2} at a current density of 15 mA cm^{-2} and 0.75 mAh cm^{-2} at a high current density of 100 mA cm^{-2}. It also exhibits high-rate capability at various current densities from 15 to 100 mA cm^{-2}

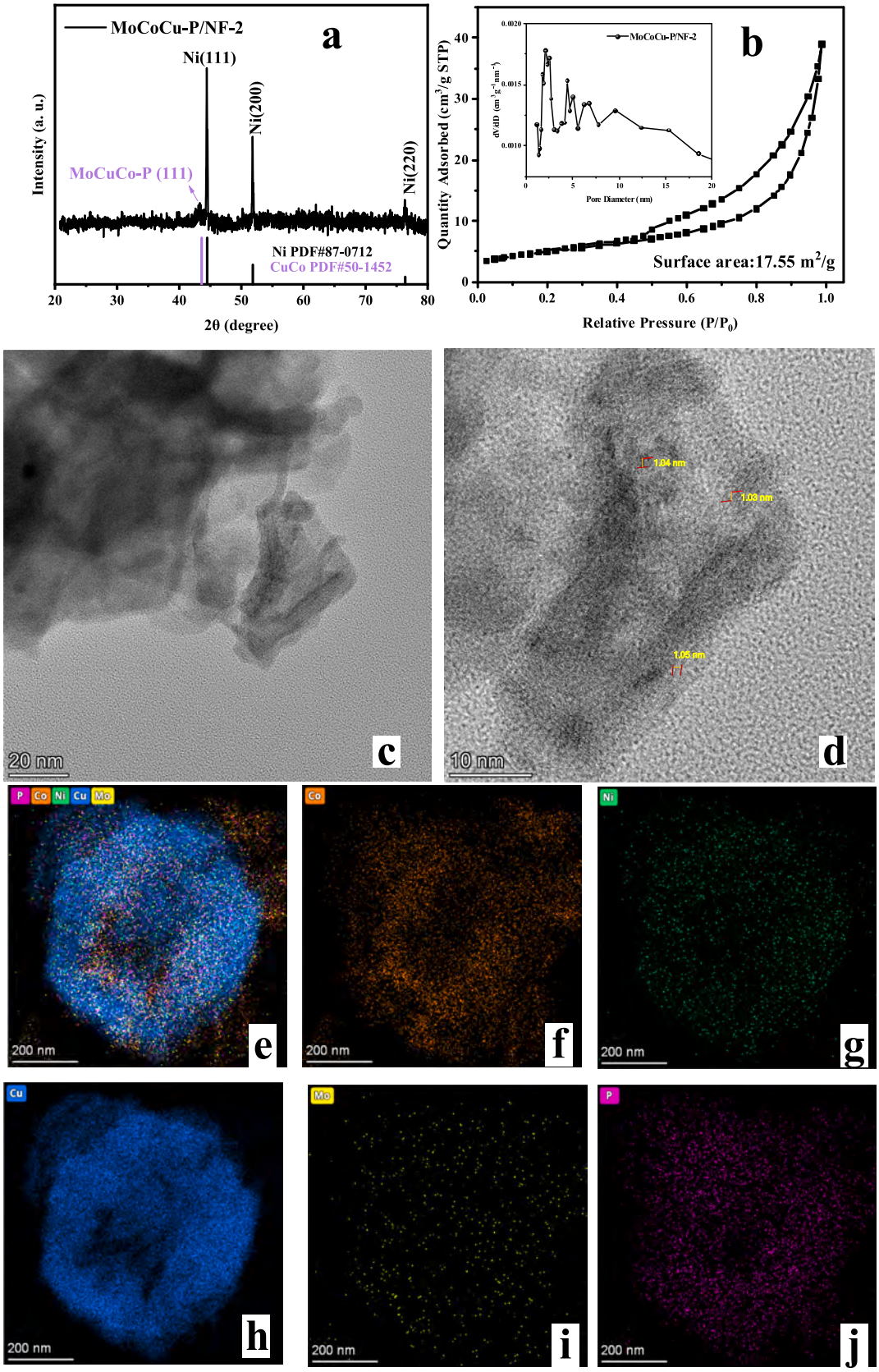

Fig. 4. Characterization of MoCoCu-P/NF-2 cathode: (a) XRD; (b) N_2 adsorption-desorption isotherms and pore size distribution (inset); (c–d) TEM; EDS elemental maps of (f) Co, (g) Ni, (h) Cu, (i) Mo, (i) P, and (e) All elements.

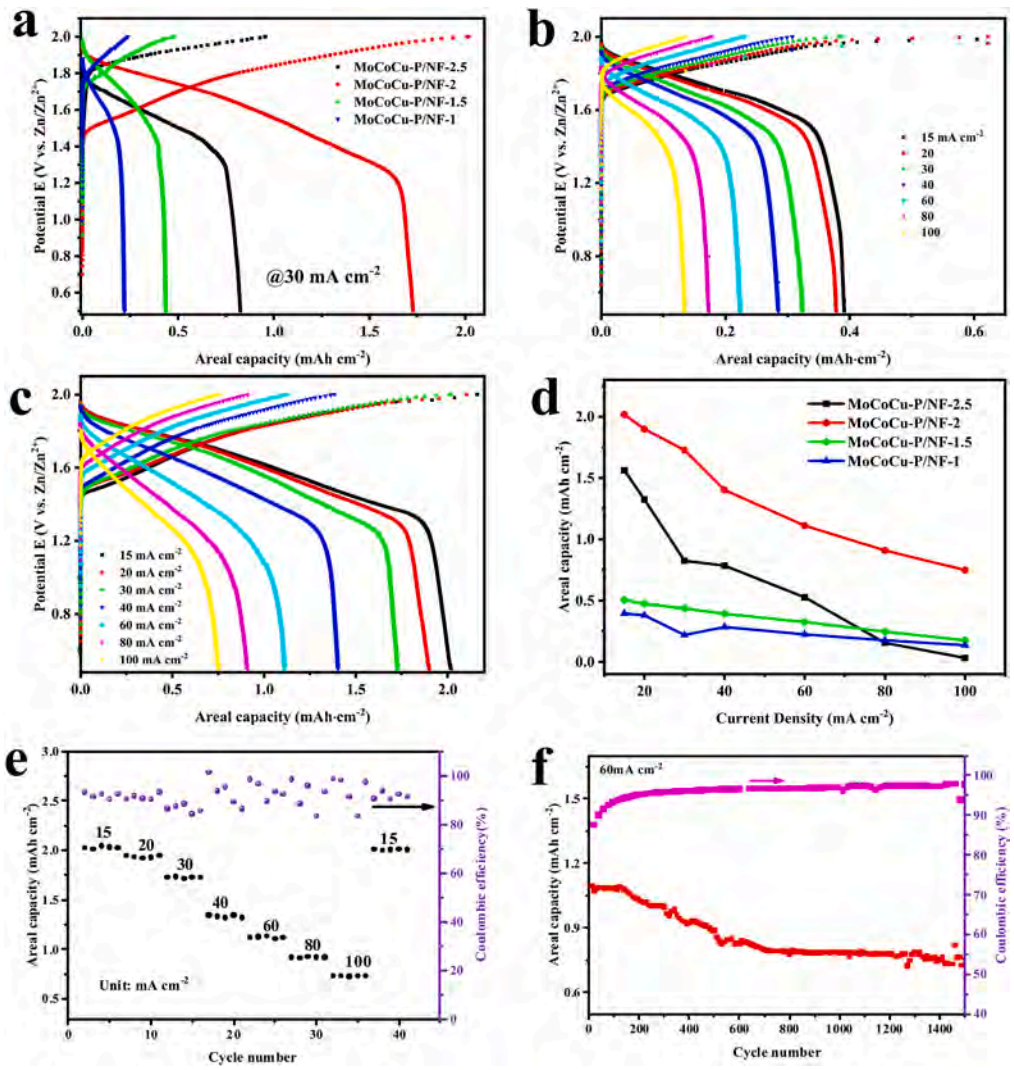

Fig. 5. Characteristics of Ni-Zn batteries composed of Zn anode and MoCoCu-P/NF cathode: (a) Charging-discharging curves of different Ni-Zn batteries at a current density of 30 mA cm^{-2}; Charging-discharging curves of Ni-Zn batteries at different current densities: (b) MoCoCu-P/NF-1 and (c) MoCoCu-P/NF-2 cathodes; (d) Areal capacities versus current densities of different Ni-Zn batteries; (e) Rate capability of the Ni-Zn battery composed of the Zn anode and MoCoCu-P/NF-2 cathode at various current densities from 15 to 100 mA cm^{-2}; (f) Cycling stability including the areal capacities and efficiencies.

together with a high CE (>90 %, Fig. 5e). For the full cell with negative deposition potential (MoCoCu-P/NF-2.5 cathode), the areal capacity is 1.6 mAh cm^{-2} at a current density 15 mA cm^{-2}, and decreases quickly with increasing current densities. The low areal capacity of 0.03 mAh cm^{-2} is observed at a current density of 100 mA cm^{-2}. Low areal capacities (<0.5 mAh cm^{-2}) are shown for positive deposition potentials (MoCoCu-P-1/NF and MoCoCu-P/NF-1.5 cathodes). Fig. 5f shows the long-term stability and cyclability of the full cell with the MoCoCu-P/NF-2 cathode (at a current density of 60 mA cm^{-2}), and the areal capacity is 1.1 mAh cm^{-2} in the initial 130 cycles, decreases to 0.85 mAh cm^{-2} in the next 600 cycles (capacity retention 80 %), and decreases to 0.76 mAh cm^{-2} in the next 900 cycles (capacity retention 89 %). The stability CE (>95 %) is maintained for 1500 cycles.

Electrochemical tests are done on the three-electrode system in 1.0 mol L^{-1} KOH, and the CV curves and EIS data are presented in Fig. 6. The oxidation peak (0.38 V vs. SCE) and reduction peak (0.21 V vs. SCE) of MoCoCu-P/NF-1 correspond to the redox process of Ni^{2+}/Ni^{3+} [43]. Owing to the low current density and narrow redox potential region, a low discharge potential (0.2 V vs. SCE) and areal capacity (0.3 mAh cm^{-2} in Supplementary Fig. S9a) correspond to the redox process of Ni substrate. The discharge voltage of the Ni-Zn full cell is 1.7 V vs. Zn/Zn^{2+}, and the areal capacity is 0.22 mAh cm^{-2} (Fig. 5a). As for the MoCoCu-P/NF-1.5 electrode, additional oxidation and reduction peaks appear at the potential 0.185 V and 0 V vs. SCE, respectively, corresponding to the redox process of Co^{2+}/Co^{3+} [44]. The redox peaks of Ni shift to the high potential in the range of 0.3–0.45 V vs. SCE. Due to the overlap of the redox process of Ni and Co, the discharge potential increases to 0.3 V vs. SCE, and the areal capacity is 0.59 mAh cm^{-2} for the three-electrode system (Supplementary Fig. S9a). The discharge voltage increases to 1.8 V, and the areal capacity increases to 0.44 mAh cm-2 for the Ni-Zn full cell (Fig. 5a). Clear oxidation and reduction peaks of Ni and Co are observed from MoCoCu-P/NF-2. Because of the larger current density and wider redox potential region, the high discharge potential (0.3 V vs. SCE) and areal capacity (0.9 mAh cm^{-2}) are obtained from the three-electrode system (Supplementary Fig. S9a). The discharge voltage of the Ni-Zn full cell is 1.8 V, and the areal capacity is 1.75 mAh cm^{-2} (Fig. 5a). MoCoCu-P/NF-2.5 does not show clear oxidation peaks of Ni and Co in the CV curves. The low current density of the oxidation and reduction peaks may be related to the low areal capacity (0.94 mAh cm^{-2}) of the three-electrode system (Supplementary Fig. S9a) and also for the Ni-Zn full cell (0.82 mAh cm^{-2}).

The CV curves acquired at different sweeping rates are shown in Fig. 6b and c for MoCoCu-P/NF-1 and MoCoCu-P/NF-2, respectively. MoCoCu-P/NF-1 shows the typical redox process of Ni^{2+}/Ni^{3+}, in which

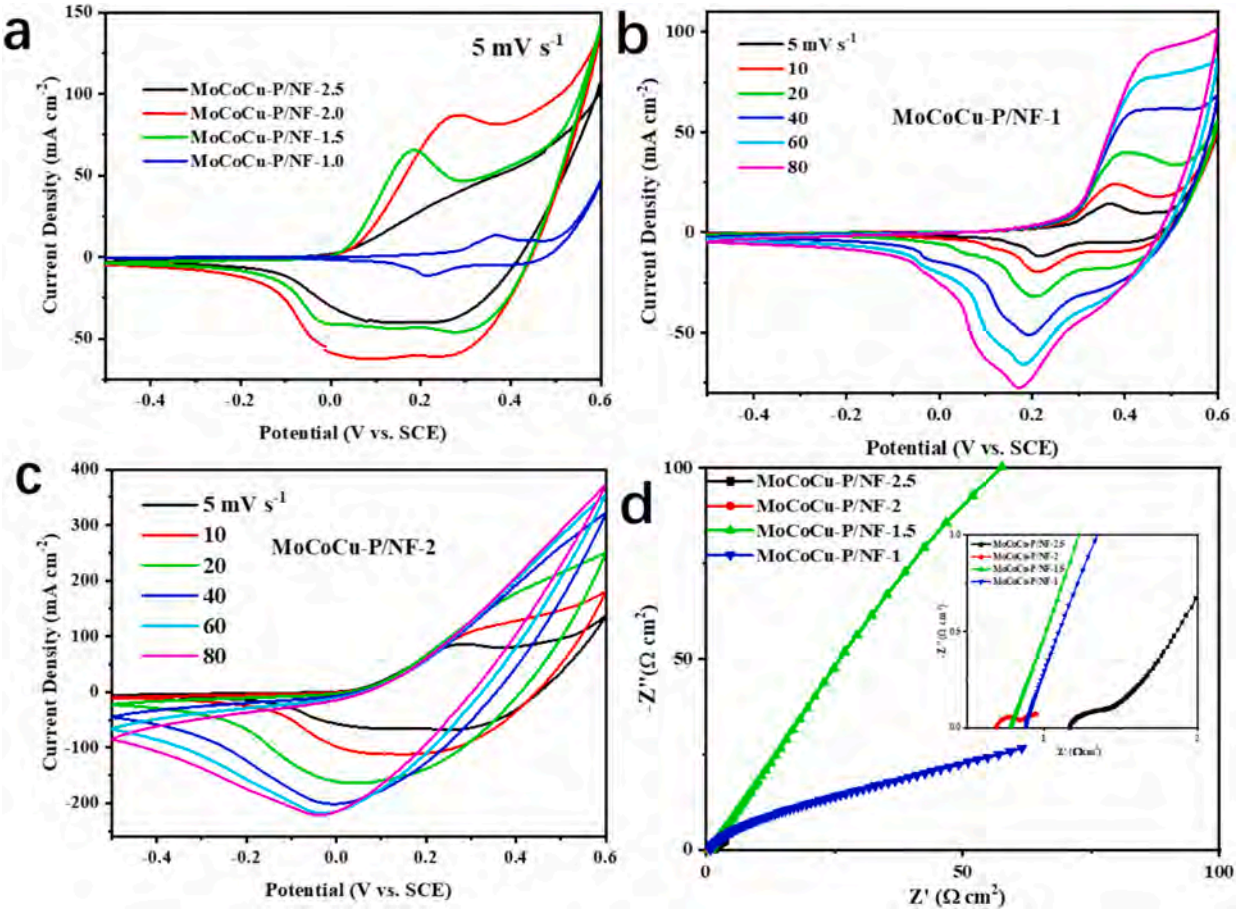

Fig. 6. Electrochemical properties of MoCoCu-P/NF cathode: (a) CV curves at a scanning rate of 5 mV s^{-1}; CV curves at different sweeping rates: (b) MoCoCu-P/NF-1 and (c) MoCoCu-P/NF-2 cathodes; (d) EIS data with inset showing the high-frequency region.

the oxidation and reduction peaks are shown at the potential 0.2 to 0.4 V, respectively, at scanning rates from 5 to 80 mV s^{-1}. Wide oxidation and reduction peaks are observed from MoCoCu-P/NF-2. The oxidation peaks appear at a potential of 0.28 V and extend to about 0.6 V vs. SCE at small sweeping rates (5–20 mV s^{-1}), and the reduction peaks begin from 0.3 V and extend to 0 V vs. SCE for small sweeping rates (5–20 mV s^{-1}). The reduction peak extends to a potential below 0 V. vs. SCE at high scanning rates (40–80 mV s^{-1}). The extended potential region and high current density correspond to the high discharge potential and areal capacity, indicating that the coating process at a suitable potential improves the discharge voltage and areal capacity. The Ni-Zn battery shows a low charge transfer resistance of 0.312 Ω cm^2 and shunt resistance of 0.698 Ω cm^2, as shown in the EIS data of MoCoCu-P/NF-2 (Fig. 6d) and fitting data in Supplementary Table S2, in addition to lower charge transfer resistance R_1 (11.82 Ω cm^2) and shunt resistance R_S (1.187 Ω cm^2) of the Ni-Zn full cell containing the Zn anode and MoCoCu-P/NF-2 cathode (Supplementary Fig. S10 and Table S3).

XPS spectra are acquired to analyze the charging and discharging processes, as shown in Fig. 7. In the initial state, Co is decoupled into Co^{2+} and Co^{3+} due to the spin-orbit doublet characteristic together with a small amount of Co^0 (Fig. 7a) [45]. The main constituent is Co^{2+}, and the Co^{2+}/Co^{3+} ratio is 3.74. Oxidation occurs after charging, as manifested by the disappearance of Co^0 and the ratio of Co^{2+}/Co^{3+} decreasing to 0.67. After discharging, the Co^{2+}/Co^{3+} ratio increases to 1.08 reflecting electron transfer and the Co redox process consistent with the electrochemical CV results for the redox process of Co^{2+}/Co^{3+}. Mo loss corresponds to the low-intensity XPS peaks after charging and discharging (Fig. 7b). After charging, the XPS peaks shift to lower binding energies (from 232.08 to 231.78 eV for Mo^{4+} and from 235.28 to 234.88 eV for Mo^{6+}), indicating easy loss of electrons [46]. After discharging, the XPS peak reverts back to the former case for Mo^{4+} (from 231.78 to 231.98 eV), together with the shift to the high binging energy for Mo^{6+} (from 234.88 to 235.88 eV). The Mo^{6+}/Mo^{4+} ratio increases from 0.677 to 0.879 after charging and decreases to 0.211 after discharging, indicative of electron transfer. The loss of Mo can be attributed to the formation of Mo^{6+} (such as MoO_4^{2-}) and dissolution in the electrolyte [47].

As shown in the P 2*p* XPS spectra (Fig. 7c), the main constituent is P^{5+}, and that of P^{5+}/P^0 ratio is 2.63 [48]. The loss of P can be identified from the decreasing XPS intensity. The P^{5+}/P^0 ratio decreases to 0.08 and 0.123 after charging and discharging, respectively. The P^0 state shows positive shifts of 0.2 eV and 0.3 eV in the charging and discharging processes, respectively, indicating decreasing electron density around P due to Ni and Co. Similar to Co, the Cu 2*p* XPS spectra show peaks of metallic and oxidation states of Cu (Fig. 7d). The Cu^0 peak shifts positively after charging (from 932.88 to 933.08 eV) and to 933.95 eV after discharging, suggesting decreasing electron density around Cu atoms due to the low electronegativity of Cu [49]. The Cu^0/Cu^{2+} ratio decreases from 0.341 to 0.242 after charging but increases to 0.5258 after discharging, implying that Cu is involved in the redox process.

In order to analysis the contribution of element in MoCoCu-P/NF-2 cathode and to identify the synergistic effect between elements, the comparing electrodes are prepared and the electrochemical CV curves are shown in Supplementary Fig. S11a. The low current densities of redox peaks are shown for the electrodes without Co or Cu elements, also corresponding to the small discharge capacities of Ni-Zn batteries (Supplementary Fig. S11b), such as MoCu-P/NF-2 and MoCo-P/NF-2. Based on the synergistic effect of Cu and Co elements, it shows the

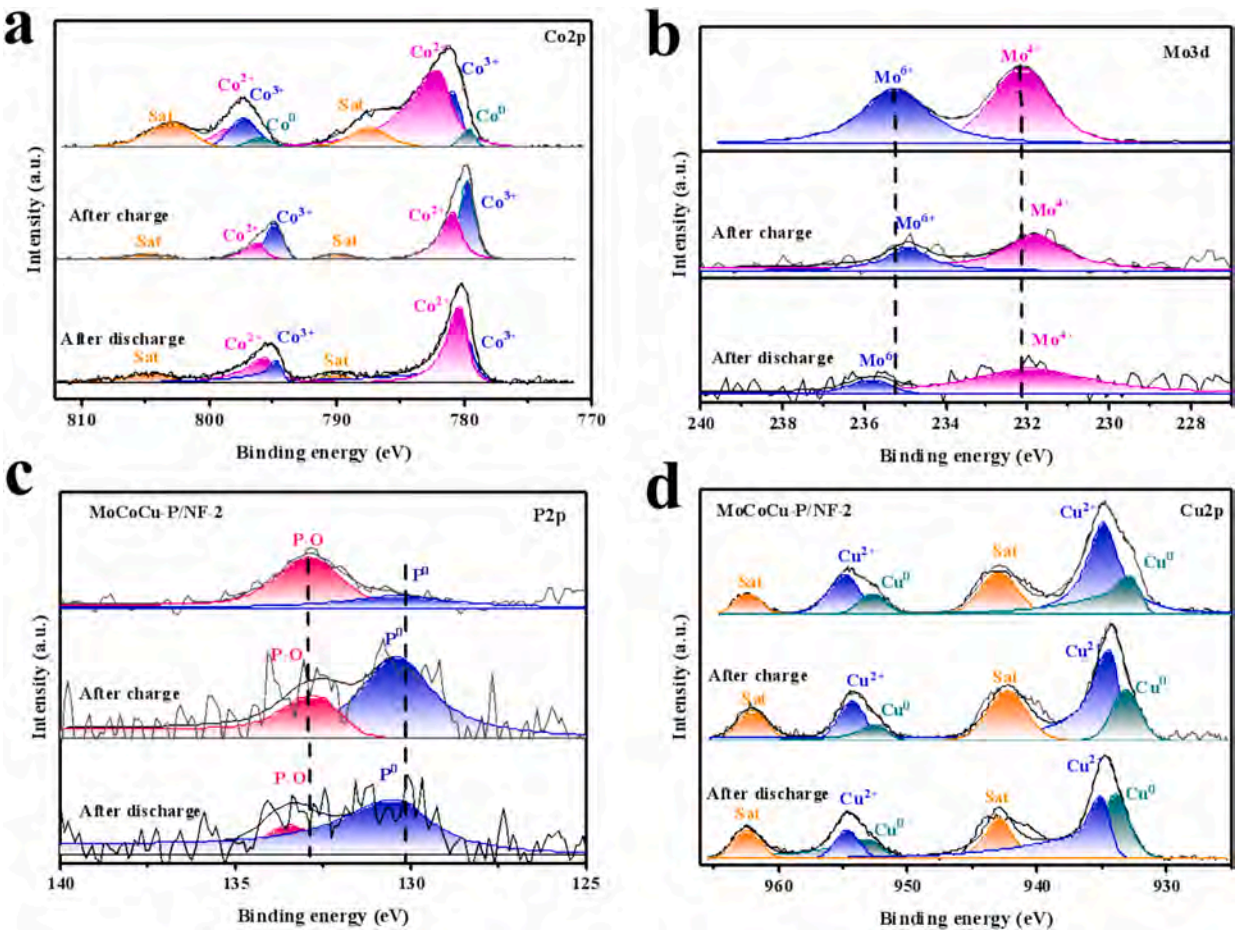

Fig. 7. XPS spectra of MoCoCu-P/NF-2 electrode after charging and discharging: (a) Co 2*p*, (b) Mo 3d, (c) P 2*p*, and (d) Cu 2*p*.

high current density of redox peaks in CV curves and large discharge capacities of Ni-Zn battery, such as CoCu-P/NF-2 and MoCoCu/NF-2 electrodes. Due to the synergistic effect between elements for MoCoCu-P/NF-2 electrode, it shows the highest current density of redox peaks in CV curve and the largest discharge capacity of Ni-Zn battery.

3.3. Ni-Zn battery composed of SiC-Zn anode and MoCoCu-P/NF-2 cathode

Ni-Zn batteries consisting of SiC-Zn anode and MoCoCu-P/NF-2 cathode are fabricated, and charging-discharging curves are obtained at different current densities (Fig. 8a), which shows the decreasing areal capacities with increasing current densities. It reveals areal capacities of 3.8 mAh cm^{-2} at a current density 20 mA cm^{-2} and 0.64 mAh cm^{-2} at a current density 90 mA cm^{-2}. The Coulombic efficiency changes from 50 % to >99 % as the current density increases from 10 to 100 mA cm^{-2}. The Coulombic efficiencies are high (>95 %) when the current densities are larger than 60 mA cm^{-2} (inset in Fig. 8a). The performance is compared to that in the literature (Supplementary Table S4). The energy density and power density are 6.25 mWh cm^{-2} and 30. 1 mW cm^{-2} at a current density 15 mA cm^{-2}, respectively, and 4.41 mWh cm^{-2} and 60.2 mW cm^{-2} can be achieved at a current density 40 mA cm^{-2}, which exceeds the majority of recently reported Ni-Zn battery.

The full cell SiC-Zn||MoCoCu-P/NF-2 shows high areal capacities at different current densities (Fig. 8b), reaching 3.5–4.0 mAh cm^{-2} at low current densities of 15 and 20 mA cm^{-2} and a low Coulombic efficiency of 70 %. The areal capacities of 1.0–2.0 mAh cm^{-2} are obtained at current densities of 30–80 mA cm^{-2} together with a high Coulombic efficiency (>90 %). The full cell can be operated for 46 h at a current density of 60 mA cm^{-2} (Fig. 8c) with a high areal capacity (>1.5 mAh cm^{-2}) in the first 200 cycles (Fig. 8d). The high performance of Ni-Zn battery would be attributed to the integrated function of SiC-coated Zn anode and MoCoCu-P medium-entropy alloy-coated Ni foam (NF) cathode, including that the synthesized SiC on the Zn foil to improve the stability of the Zn anode, and electrodeposited MoCoCu-P on the NF to improve the capacity of the Ni-Zn battery.

The MoCoCu-P/NF cathode is analyzed after cycling. The oxidation states of Cu (CuO) of MoCoCu-P/NF-2 and Ni substrate are determined by XRD (Supplementary Fig. S12a) [50]. Raman scattering is performed after cycling and it also shows oxidation of the CuCo alloy during charging-discharging (Supplementary Fig. S12b). During the charge-discharge process of the Ni-Zn battery, Mo dissolves in the solution, and Raman scattering reveals CuO and Co_3O_4 [51,52]. The surface morphologies after cycling are depicted in Fig. 8e–g, suggesting that the spherical structure composed of nanowires can keep the redox process in the Ni-Zn battery.

4. Conclusions

A high-performance nickel-zinc alkaline battery composed of the SiC-coated Zn anode and MoCoCu-P medium-entropy alloy-coated Ni foam (NF) cathode is designed and fabricated. The areal capacity, energy (power) density, and cycling stability are enhanced by SiC deposition, which improves Zn plating/stripping. The CoMoCu-P medium-entropy alloy on NF improves the capacity and cycling stability because of the synergistic effects rendered by the different metals and hybrid redox process of Ni and Co. The battery shows a large areal capacity 4.0 mAh cm^{-2} (15.0 mA cm^{-2}), and excellent cyclability for 45 h (areal

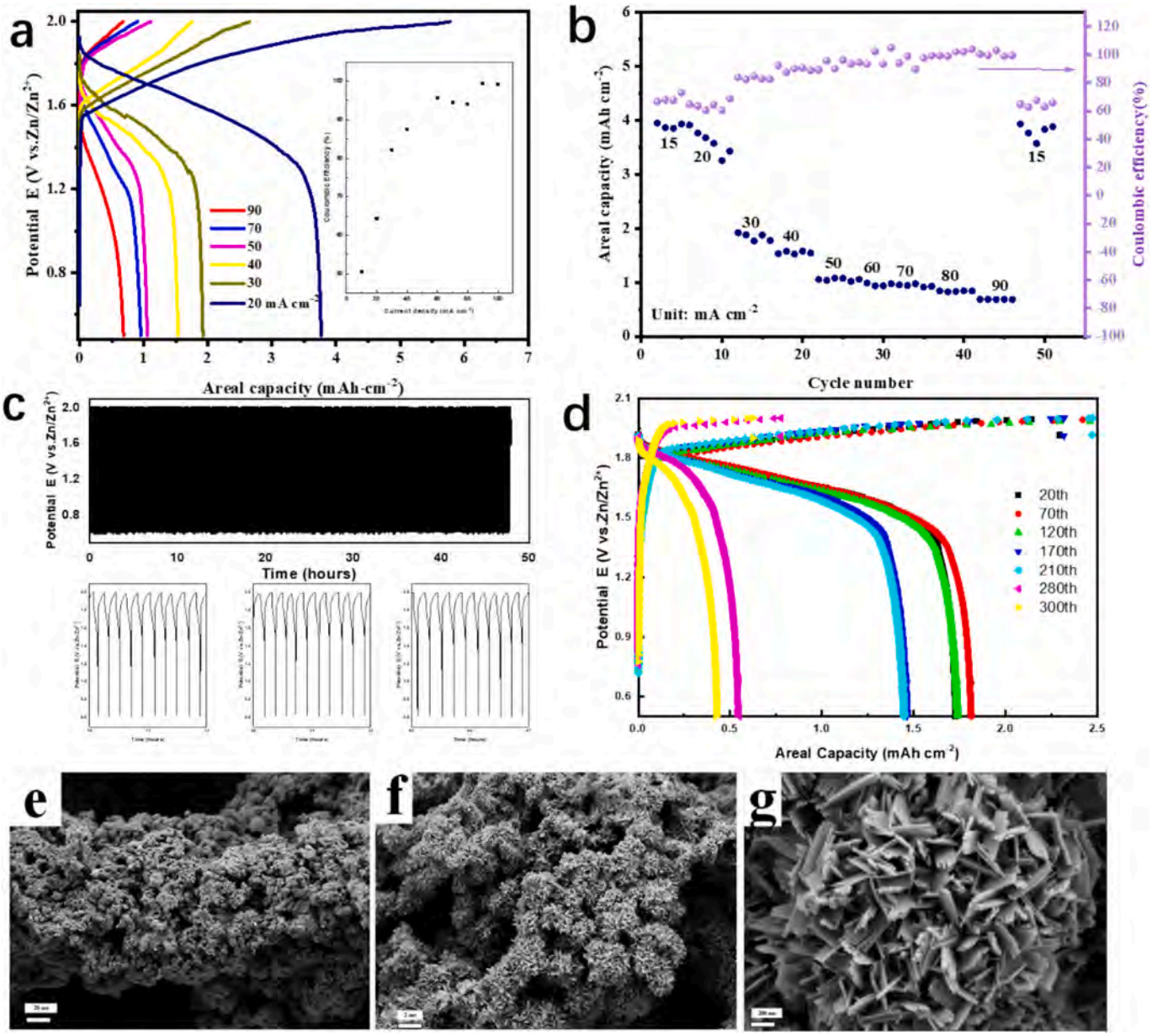

Fig. 8. Properties of Ni-Zn batteries with SiC-Zn anode and MoCoCu-P/NF-2 cathode: (a) Charging-discharging curves at various current densities from 20 to 90 mA cm^{-2} with the inset showing the Coulombic efficiency versus current densities; (b) Rate capability at various current densities from 15 to 90 mA cm^{-2}; (c) Cycling stability in the initial 300 cycles at a current density of 60 mA cm^{-2}; (d) Charging-discharging curves for different cycle numbers. (e–g) SEM images of MoCoCu-P/NF-2 cathode after testing.

capacity 1.5 mAh cm^{-2} at 60.0 mA cm^{-2}). The energy density and power density are 6.25 (4.41) mWh cm^{-2} and 31.1 (60.2) mW cm^{-2}, respectively, at a current density of 15 (40) mA cm^{-2}. All in all, the excellent properties of the Ni-Zn alkaline battery arise from the improved Zn plating/stripping process and SiC coating, synergistic effects rendered by the different ingredients, as well as the hybrid redox process of Ni and Co.

CRediT authorship contribution statement

Caijin Yang: Formal analysis, Data curation. **Xue Wang:** Formal analysis, Data curation. **Dajun Wu:** Project administration, Formal analysis. **Fanya Jin:** Investigation, Formal analysis. **Zhenzhong Yang:** Formal analysis, Data curation. **Shaohui Xu:** Project administration. **Dayuan Xiong:** Funding acquisition, Formal analysis. **Lianwei Wang:** Project administration, Formal analysis. **Paul K. Chu:** Writing – review & editing, Funding acquisition.

Declaration of competing interest

We declare that we have no financial and personal relationships with other people or organizations that can inappropriately influence our work, there is no professional or other personal interest of any nature or kind in any product, service and/or company that could be construed as influencing the position presented in, or the review of, the manuscript entitled.

Acknowledgments

This work was jointly supported by the National Natural Science Foundation of China (No. 61176108), Research Innovation Foundation of ECNU (No. 78210245), and City University of Hong Kong Donation

Research Grant (DON-RMG No. 9229021).

Appendix A. Supplementary data

Supplementary data to this article can be found online at https://doi.org/10.1016/j.est.2024.114934.

Data availability

No data was used for the research described in the article.

References

[1] D. Chao, W. Zhou, F. Xie, C. Ye, H. Li, M. Jaroniec, S. Qiao, Roadmap for advanced aqueous batteries: from design of materials to applications, Sci. Adv. 6 (2020) eaba4098 (1 to 19).

[2] Y. Deng, R. Liang, G. Jiang, Y. Jiang, A. Yu, Z. Chen, The current state of aqueous Zn-based rechargeable batteries, ACS Energy Lett. 5 (2020) 1665–1675.

[3] L. Tang, H. Peng, J. Kang, H. Chen, et al., Zn-based batteries for sustainable energy storage: strategies and mechanisms, Chem. Soc. Rev. 53 (2024) 4877–4925.

[4] J.F. Parker, C.N. Chervin, I.R. Pala, M. Machler, et al., Rechargeable nickel–3D zinc batteries: an energy-dense, safer alternative to lithium-ion, Science 356 (2017) 415–418.

[5] F. Wang, O. Borodin, T. Gao, X. Fan, et al., Highly reversible zinc metal anode for aqueous batteries, Nat. Mater. 17 (2018) 543–549.

[6] L. Ma, M.A. Schroeder, O. Borodin, et al., Realizing high zinc reversibility in rechargeable batteries, Nat. Energy 5 (2020) 743–749.

[7] J. Zheng, Q. Zhao, T. Tang, J. Yin, et al., Reversible epitaxial electrodeposition of metals in battery anodes, Science 366 (2019) 645–648.

[8] X. Zhang, Q. Shen, X. Lin, C. Luo, et al., Ion-confinement effect for zinc anode of aqueous zinc ion batteries, J. Energy Storage 73 (2023) 109085.

[9] J. Wu, W. Xu, Z. Wu, J. Wan, et al., Triethanolamine-modified binder with synergistic effects on Zn anode in improving the cycling stability of aqueous rechargeable Zn-Ni batteries, J. Energy Storage 72 (2023) 108430.

[10] P. Chen, X. Yuan, Y. Xia, et al., An artificial polyacrylonitrile coating layer confining zinc dendrite growth for highly reversible aqueous zinc-based batteries, Adv. Sci. 8 (2021) 2100309 (1 to 9).

[11] H. Yu, Y. Zeng, N. Li, D. Luan, et al., Confining Sn nanoparticles in interconnected N-doped hollow carbon spheres as hierarchical zincophilic fibers for dendrite-free Zn metal anodes, Sci. Adv. 8 (2022) eabm5766 (1 to 9).

[12] B. Ren, S. Hu, A. Chen, X. Zhang, H. Wei, et al., Inhibiting dendrite formation and electrode corrosion via a scalable self-assembled Mercaptan layer for stable aqueous zinc batteries, Adv. Energy Mater. 14 (2024), 2302970 (1 to 11).

[13] J. Zheng, G. Zhu, X. Liu, H. Xie, et al., Simultaneous dangling bond and zincophilic site engineering of SiN_X protective coatings toward stable zinc anodes, ACS Energy Lett. 7 (2022) 4443–4450.

[14] M. Zhou, S. Guo, J. Li, X. Luo, et al., Surface-preferred crystal plane for a stable and reversible zinc anode, Adv. Mater. 33 (2021), 2100187 (1 to 9).

[15] S. Chen, Y. Xia, R. Zeng, Z. Luo, X. Wu, et al., Ordered planar plating/stripping enables deep cycling zinc metal batteries, Sci. Adv. 10 (2024) eadn2265 (1 to 12).

[16] J. Zheng, L.A. Archer, Controlling electrochemical growth of metallic zinc electrodes: toward affordable rechargeable energy storage systems, Sci. Adv. 7 (2021) eabe0219. (1 to 19).

[17] D. Selvakumaran, A. Pan, S. Liang, G. Cao, A review on recent developments and challenges of cathode materials for rechargeable aqueous Zn-ion batteries, J. Mater. Chem. A 7 (2019) 18209–18236.

[18] J. Islam, R. Anwar, M. Shareef, H.M. Zabed, et al., Rechargeable metal-metal alkaline batteries: recent advances, current issues and future research strategies, J. Power Sources 563 (2023) 232777.

[19] X. Zhang, J. He, L. Zhou, H. Zhang, Q. Wang, et al., Ni (II) coordination supramolecular grids for aqueous nickel-zinc battery cathodes, Adv. Funct. Mater. 31 (2021), 2100443 (1 to 10).

[20] P. Hu, T. Wang, J. Zhao, C. Zhang, et al., Ultrafast alkaline Ni/Zn battery based on Ni-foam-supported Ni_3S_2 nanosheets, ACS Appl. Mater. Interfaces 7 (2015) 26396–26399.

[21] Y. Zhou, X. Tong, N. Pang, Y. Deng, et al., Ni_3S_2 nanocomposite structures doped with Zn and Co as long-lifetime, high-energy-density, and binder-free cathodes in flexible aqueous nickel-zinc batteries, ACS Appl. Mater. Interfaces 13 (2021) 34292–34300.

[22] Z. Wang, P. Shi, Q. Liu, J. Li, et al., Enhanced polymerization interface of $Ni_{12}P_5$ nanowires toward high-rate and durable cathode for alkaline Ni-Zn batteries, J. Power Sources 550 (2022) 232170.

[23] R. Zhang, S. Zhao, J. Ding, Y. Chong, et al., Short-range order and its impact on the CrCoNi medium-entropy alloy, Nature 581 (2020) 283–287.

[24] X. Chen, Q. Wang, Z. Cheng, M. Zhu, et al., Direct observation of chemical short-range order in a medium-entropy alloy, Nature 592 (2021) 712–716.

[25] Y. Ma, Y. Ma, Q. Wang, S. Schweidler, et al., High-entropy energy materials: challenges and new opportunities, Energ. Environ. Sci. 14 (2021) 2883–2905.

[26] T. Jang, W. Choi, D. Kim, et al., Shear band-driven precipitate dispersion for ultrastrong ductile medium-entropy alloys, Nat. Commun. 12 (2021) 4703.

[27] Y. Yang, Z. Jia, X. Zhang, Y. Liu, et al., Chemical short-range order in multi principal element alloy with ordering effects on water electrolysis performance, Mater. Today 72 (2024) 97–108.

[28] X. Wang, C. Yang, Y. Zhang, D. Xiong, S. Xu, et al., Medium-entropy alloy MoCoCu-P as an efficient bifunctional catalyst for water splitting, J. Alloy. Compd. 988 (2024), 174332 (1 to 11).

[29] Y. Wei, R. Yao, X. Liu, W. Chen, et al., Understanding the configurational entropy evolution in metal-phosphorus solid solution for highly reversible Li-ion batteries, Adv. Sci. 10 (9) (2023) 2300271.

[30] M. Li, L. Zong, J. Zhao, et al., The millisecond fabrication of medium-entropy alloy as a high-performance bifunctional electrocatalyst for ultralong-term rechargeable zinc-air batteries, J. Alloy. Compd. 976 (2024) 173183.

[31] P. Wang, S. Liang, C. Chen, X. Xie, et al., Spontaneous construction of nucleophilic carbonyl-containing interphase toward Ultrastable zinc-metal anodes, Adv. Mater. 34 (2022), 2202733 (1 to 8).

[32] F. Chang, J. Zheng, X. Wang, Q. Xu, et al., Heterojuncted non-metal binary composites silicon carbide/g-C_3N_4 with enhanced photocatalytic performance, Mater. Sci. Semicon. Proc. 75 (2018) 183–192.

[33] Y. Wang, Z. Zheng, J. Wang, X. Liu, et al., New method for preparing ZnO layer for efficient and stable organic solar cells, Adv. Mater. 35 (2023), 2208305 (1 to 8).

[34] B. Li, J. Quan, A. Loh, J. Chai, et al., A robust hybrid Zn-battery with ultralong cycle life, Nano Lett. 17 (2017) 156–163.

[35] Q. Li, A. Chen, D. Wang, Z. Pei, C. Zhi, "Soft shorts" hidden in zinc metal anode research, Joule 6 (2021) 269–279.

[36] V. Augustyn, J. Come, M.A. Lowe, J.W. Kim, et al., High-rate electrochemical energy storage through Li^+ intercalation pseudocapacitance, Nat. Mater. 12 (2013) 518–522.

[37] M.E. Orazem, B. Tribollrt, Electrochemical Impedance Spectroscopy, by John Wiley & Sons, Inc, Hoboken, New Jersey, 2008.

[38] Z. Lukács, T. Kristóf, A generalized model of the equivalent circuits in the electrochemical impedance spectroscopy, Electrochim. Acta 363 (2020), 137199 (1 to 11).

[39] J. Lu, T. Xiong, W. Zhou, L. Yang, Z. Tang, S. Chen, Metal nickel foam as an efficient and stable electrode for hydrogen evolution reaction in acidic electrolyte under reasonable overpotentials, ACS Appl. Mater. Interfaces 8 (2016) 5065–5069.

[40] T. Fu, X. Tong, Y. Zhou, D. Wu, D. Xiong, et al., One-step hydrothermal synthesis of CoNi bimetallic phosphide nanoflowers for high-performance quasi-solid-state zinc-ion batteries, J. Alloy. Compd. 918 (2022) 165734.

[41] J. Fang, Q. Zheng, Y. Lou, K. Zhao, et al., Ampere-level current density ammonia electrochemical synthesis using CuCo nanosheets simulating nitrite reductase bifunctional nature, Nat. Commun. 13 (2022) 7899.

[42] E.P. George, D. Raabe, R.O. Ritchie, High-entropy alloys, Nat. Rev. Mater. 4 (2019) 515–534.

[43] G. Barral, F. Njanjo-Eyoke, S. Maximovitch, Characterization of the passive layer and of hydroxide deposits of nickel by impedance spectroscopy, Electrochim. Acta 40 (1995) 2815.

[44] W. Luo, H. Tian, Q. Li, G. Meng, et al., Controllable electron distribution reconstruction of spinel $NiCo_2O_4$ boosting glycerol oxidation at elevated current density, Adv. Funct. Mater. 34 (2024) 2306995.

[45] P. Gao, Y. Zeng, P. Tang, Z. Wang, et al., Understanding the synergistic effects and structural evolution of $Co(OH)_2$ and Co_3O_4 toward boosting electrochemical charge storage, Adv. Funct. Mater. 32 (2022), 2108644 (1 to 13).

[46] Y. Yan, S. Liang, X. Wang, et al., Robust wrinkled MoS_2/N-C bifunctional electrocatalysts interfaced with single Fe atoms for wearable zinc-air batteries, Proc. Natl. Acad. Sci. U. S. A. 118 (2021) e211003611 (1 to 8).

[47] L. Shao, X. Han, L. Shi, T. Wang, et al., In situ generation of molybdate-modulated nickel-iron oxide electrodes with high corrosion resistance for efficient seawater electrolysis, Adv. Energy Mater. 14 (2024), 2303261 (1 to 10).

[48] L. Yang, X. Cao, X. Wang, Q. Wang, L. Jiao, Regulative electronic redistribution of $CoTe_2$/CoP heterointerfaces for accelerating water splitting, Appl. Catal. Environ. 329 (2023) 122551.

[49] M.C. Biesinger, Advanced analysis of copper X-ray photoelectron spectra, Surf. Interface Anal. 49 (2017) 1325–1334.

[50] J. Meng, Z. Yang, L. Chen, H. Qin, et al., Energy storage performance of CuO as a cathode material for aqueous zinc ion battery, Mater. Today Energy 15 (2020) 100370.

[51] H. Xin, L. Lin, R. Li, D. Li, et al., Overturning CO_2 hydrogenation selectivity with high activity via reaction-induced strong metal-support interactions, J. Am. Chem. Soc. 144 (2022) 4874–4882.

[52] D. Yan, R. Chen, Z. Xiao, S. Wang, Engineering the electronic structure of Co_3O_4 by carbon-doping for efficient overall water splitting, Electrochim. Acta 303 (2019) 316–322.

High-performance nickel-zinc battery composed of SiC-coated zinc anode and MoCoCu-P coated nickel foam cathode

Caijin Yang[a,1], Xue Wang[a,1], Dajun Wu [b*], Fanya Jin[c], Zhenzhong Yang[a], Shaohui Xu[a,d*], Dayuan Xiong [a], Lianwei Wang[a], and Paul K. Chu[d]

[a] Key Laboratory of Polar Materials and Devices, Ministry of Education, and School of Physics and Electronic Science, East China Normal University, 500 Dongchuan Road, Minhang District, Shanghai, 200241, China

[b] Jiangsu Laboratory of Advanced Functional Materials, School of Electronic and Information Engineering, Changshu Institute of Technology, Changshu 215500, China

[c] Southwest Institute of Physics of Nuclear Industry, Chengdu 610041,China

[d] Department of Physics, Department of Materials Science & Engineering, and Department of Biomedical Engineering, City University of Hong Kong, Tat Chee Avenue, Kowloon, Hong Kong, China

*Authors to whom correspondence should be addressed:

shxu@ee.ecnu.edu.cn (Shaohui Xu); **201700028@cslg.edu.cn** (Dajun Wu), Tel.: +86 21 54342501; Fax: +86 21 54345119

[1] These authors contributed to the work equally and should be regarded as co-first authors.

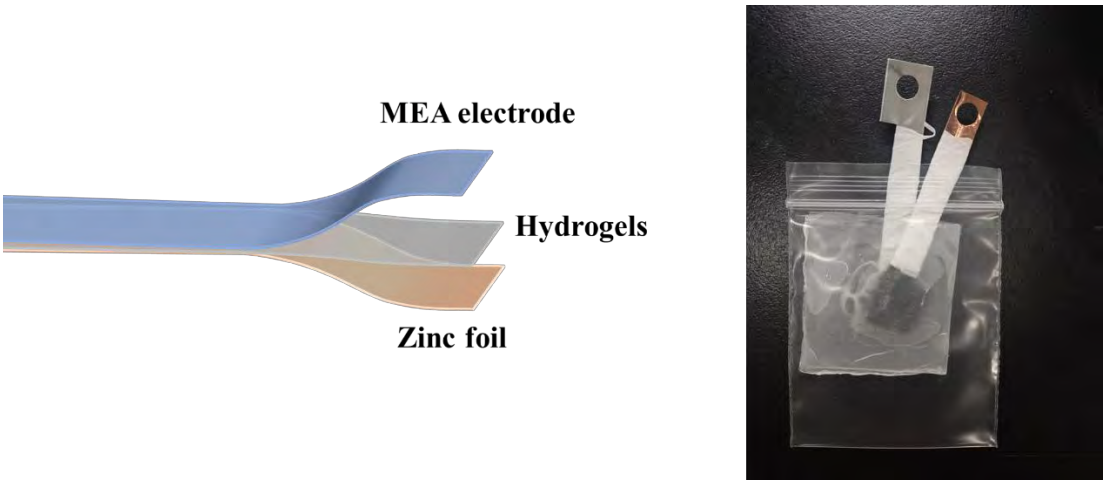

Fig. S1 Schematic and photograph of flexible Ni-Zn battery.

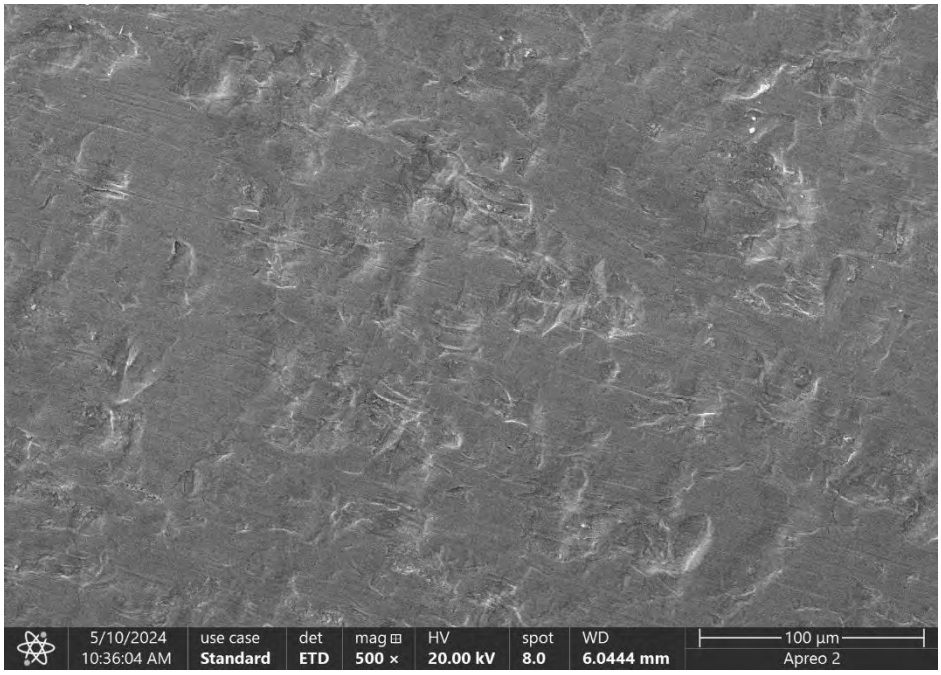

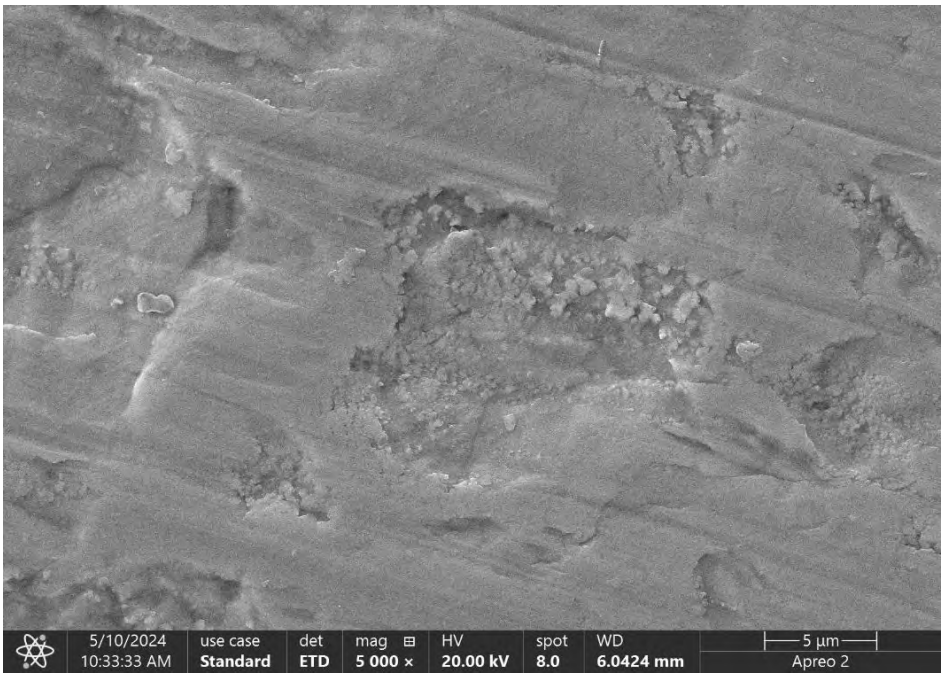

Figure S2 SEM images of SiC-coated Zn foil.

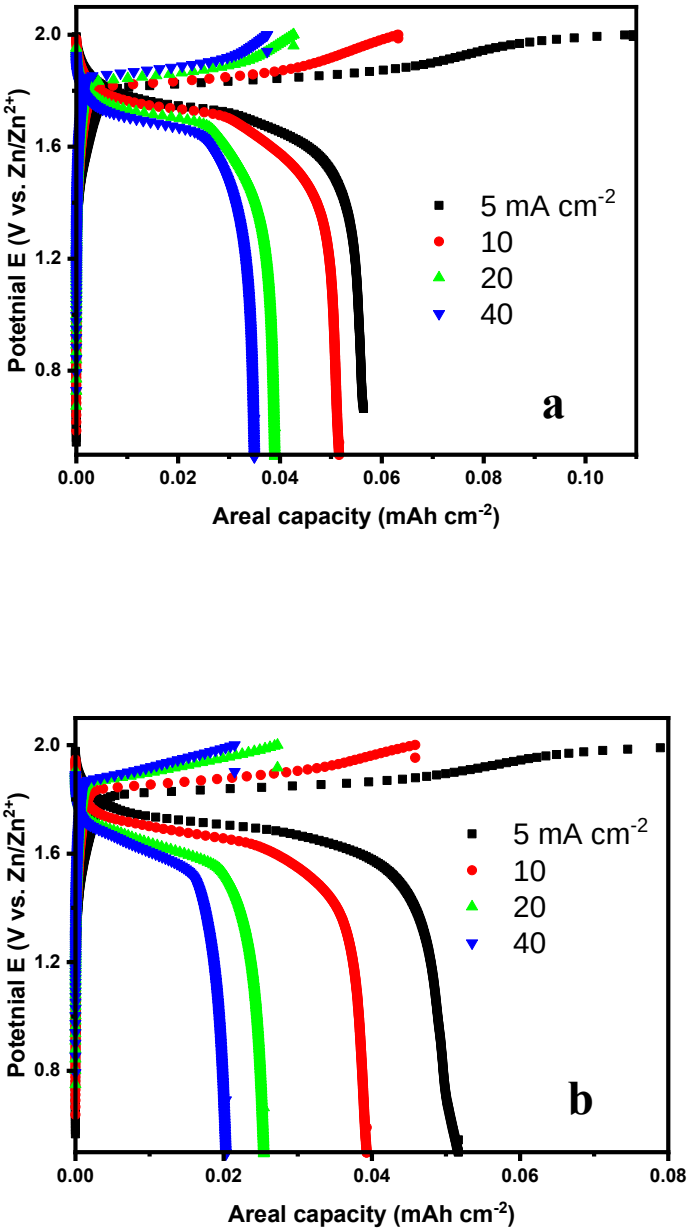

Figure S3 Charging-discharging curves acquired at different current densities from Ni-Zn batteries (5 to 40 mA cm^{-2}) with NF cathode: (a) Zn and (b) OA-Zn anode.

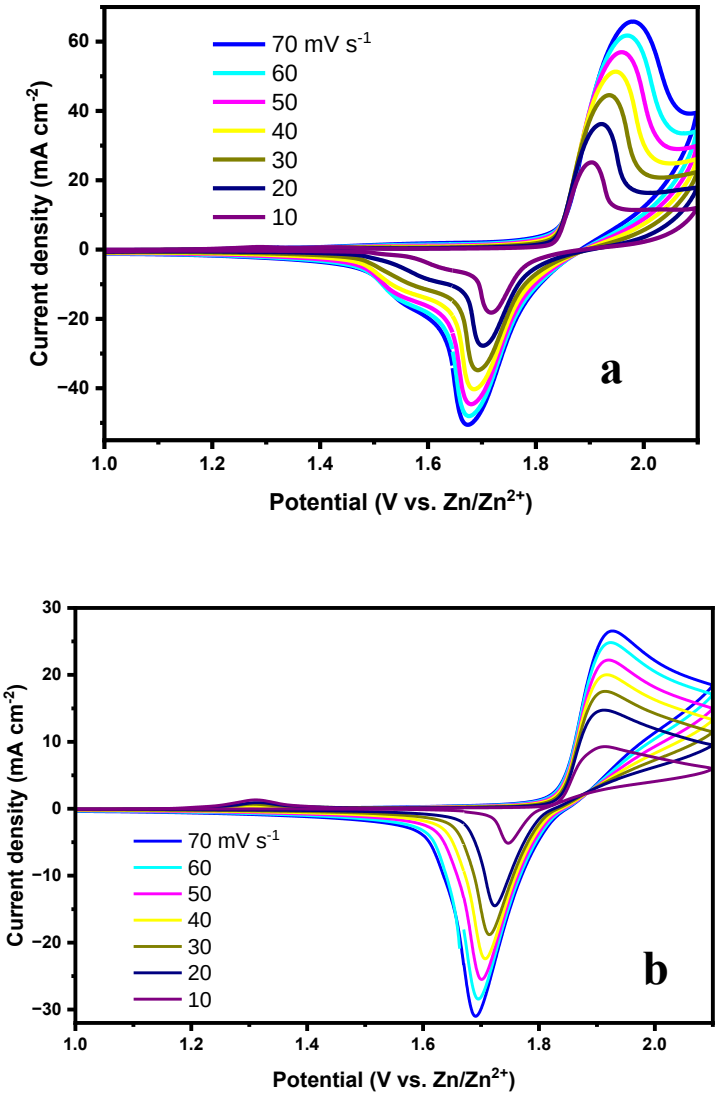

Figure S4 CV curves of the Ni-Zn full cell in the high potential region (Ni redox region) with the NF cathode: (a) Zn and (b) OA-Zn anode.

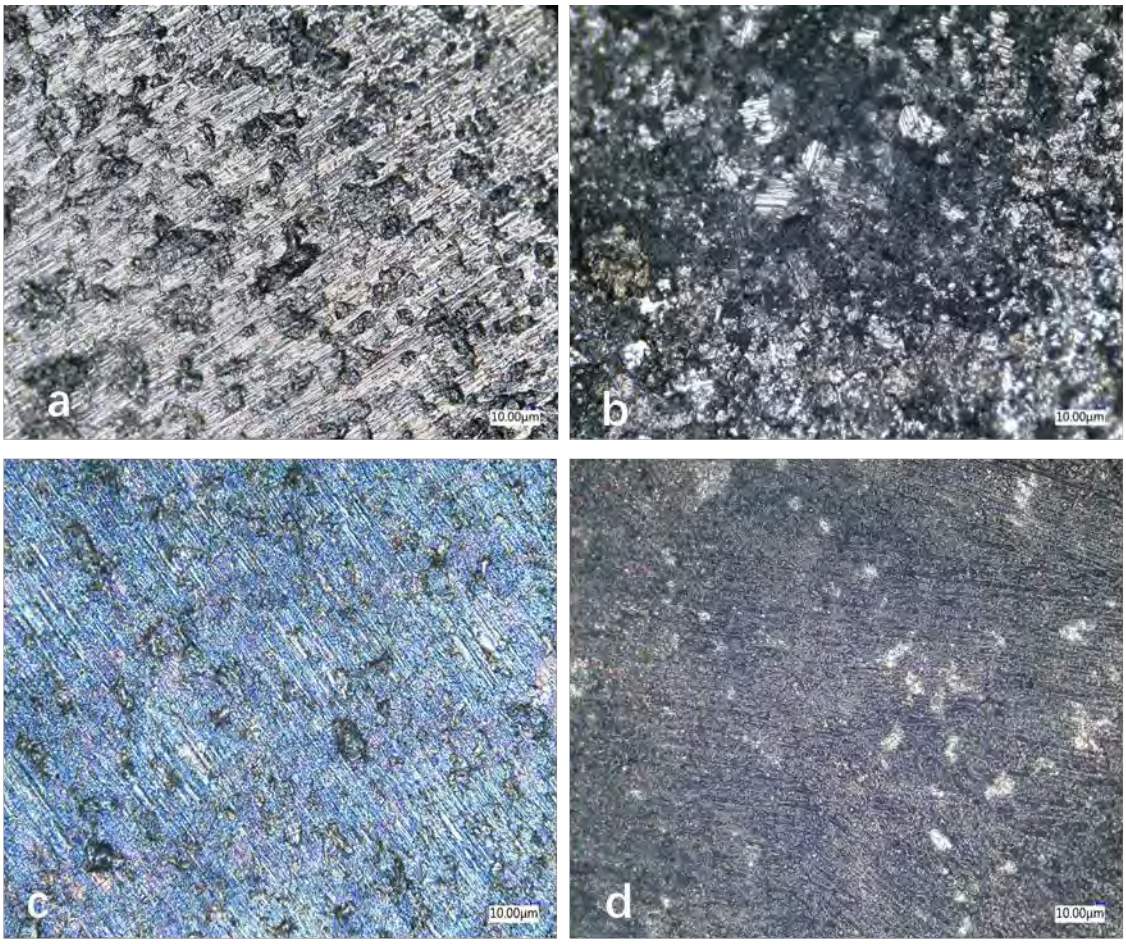

Figure S5 Optical micrographs before (left) and after (right) test in 1.0 mol L^{-1} KOH solution: (a, b) Zn foil and (c, d) SiC-Zn.

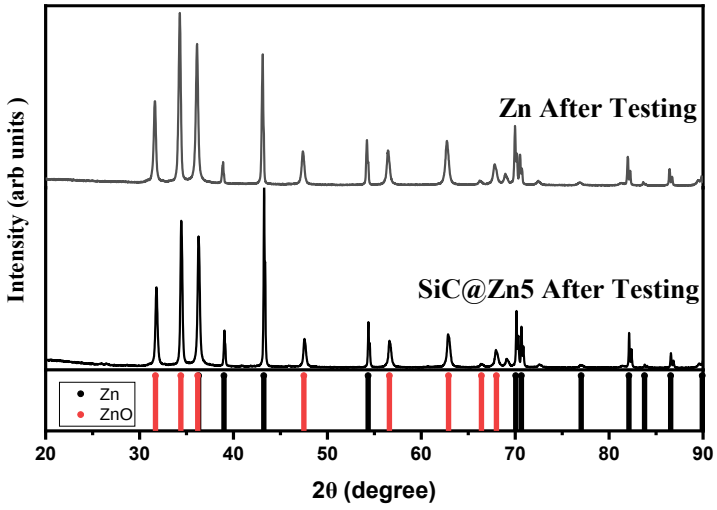

Figure S6 XRD pattern of Zn foil and SiC-Zn after test in 1.0 mol L^{-1} KOH solution.

Table S1 Load of MoCoCu-P deposited on NF electrode at potential -2.0 V vs. SCE.

Time	10 min	20 min	40 min	80 min
Before	0.0203	0.0205	0.0185	0.0193
After	0.0225	0.0254	0.0359	0.0489
load（g/cm^2）	0.0022	0.0049	0.0174	0.0295

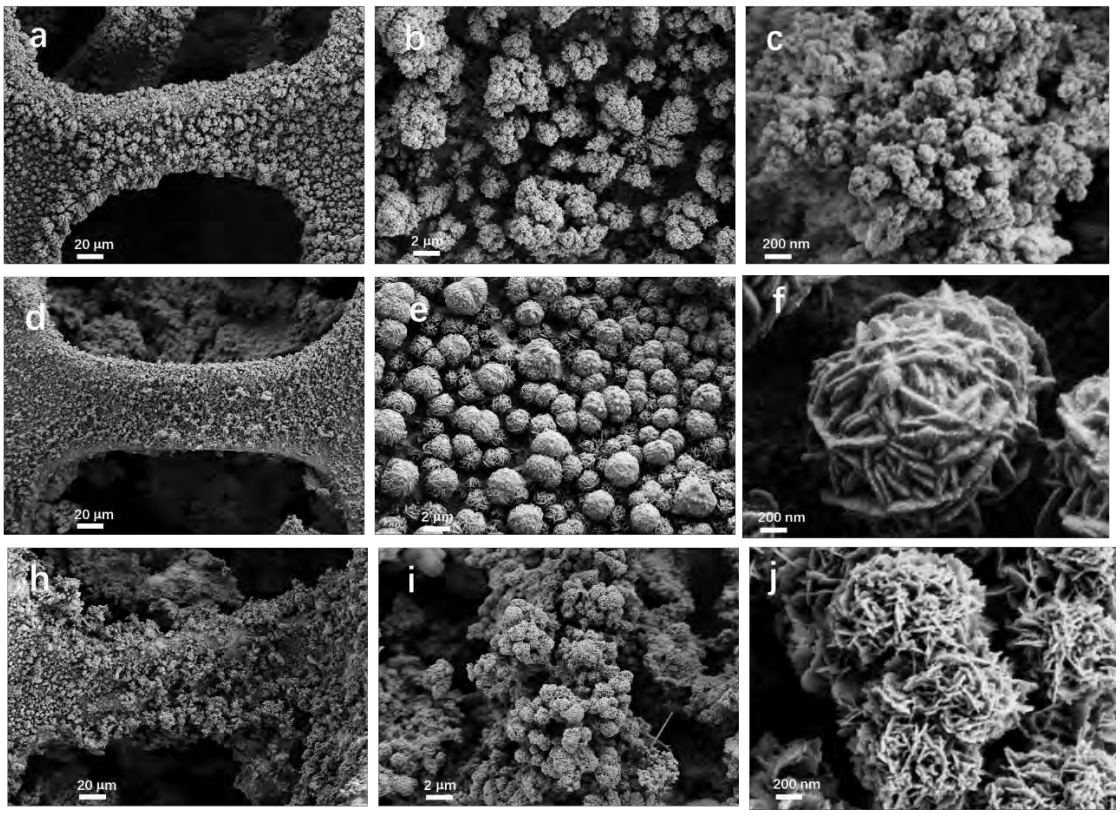

Figure S7 SEM images of MoCoCu-P coated NF deposited at the different potential. (a-c) MoCoCu-P/NF-1, (d-f) MoCoCu-P/NF-2, (h-i) MoCoCu-P/NF-2.5.

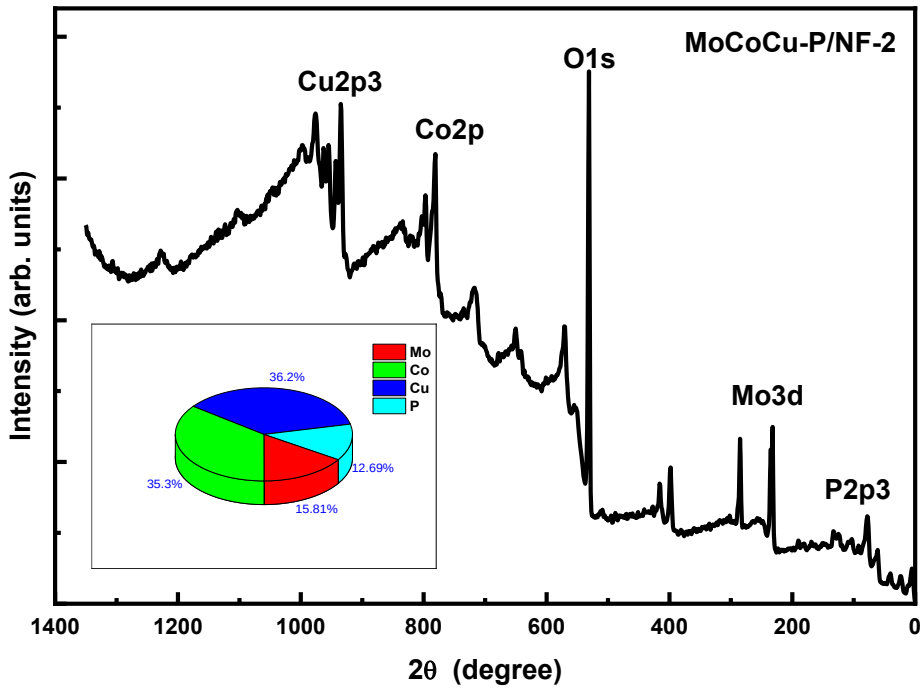

Figure S8 XPS spectrum and elemental composition of MoCoCu-P/NF-2.

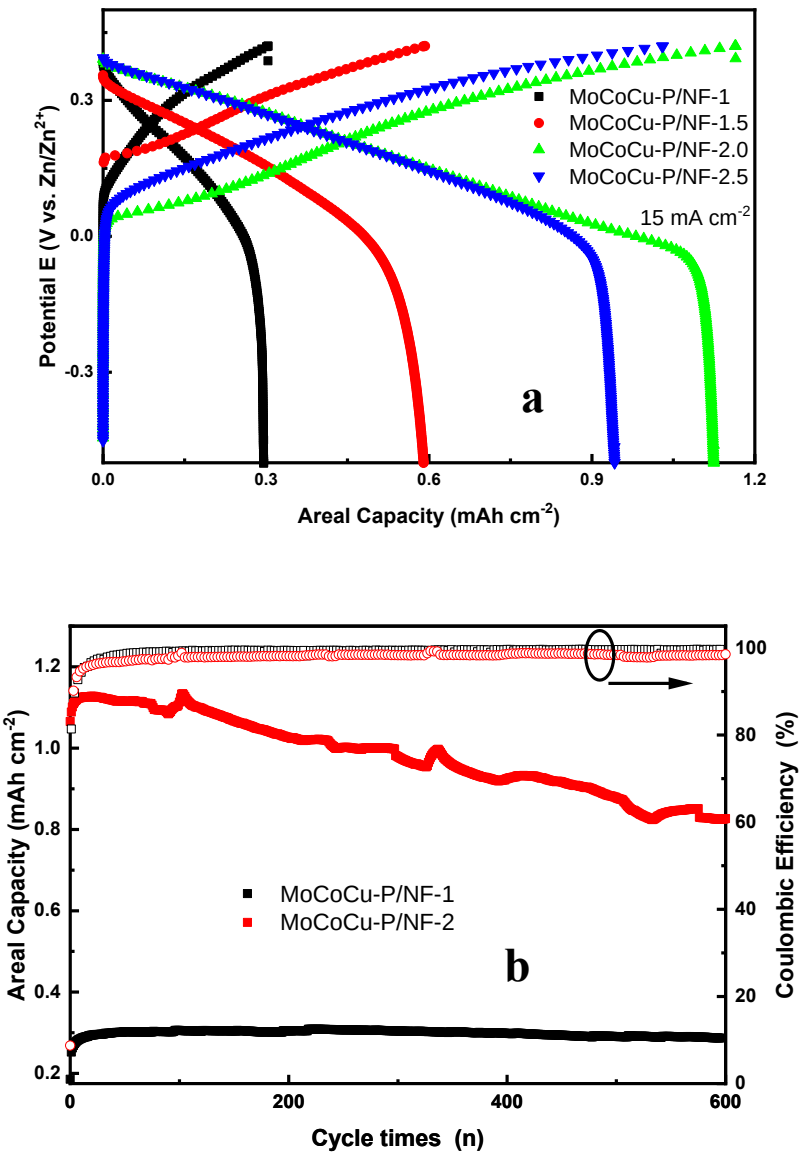

Figure S9 Electrochemical properties of the MoCoCu-P/NF electrode in 1 mol L^{-1} KOH solution for three-electrode measurement: (a) Charging-discharging curves at a current density of 15 mA cm^{-2}, (b) Cycle stability for 600 cycles showing the areal capacity and Coulombic efficiency.

Table S2 Electrochemical impedance spectra fitting data at the open circuit potential (OCP) of the MoCoCu-P/NF electrodes deposited at different potentials.

Samples	R_s（Ω cm^2）	R_1（Ω cm^2）
MoCoCu-P/NF-1	0.958	5.821
MoCoCu-P/NF-1.5	0.790	16.11
MoCoCu-P/NF-2	0.698	0.312
MoCoCu-P/NF-2.5	1.144	0.545

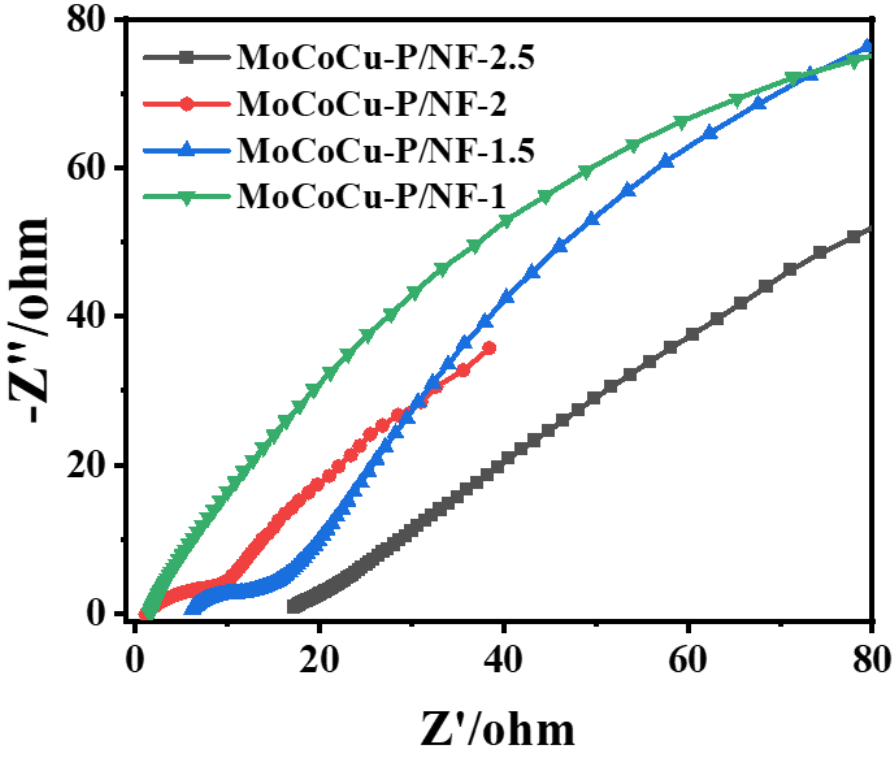

Figure S10 Electrochemical impedance spectra (EIS) of Ni-Zn batteries composed of the Zn anode and MoCoCu-P/NF cathodes.

Table S3 Electrochemical impedance spectra fitting data at the open circuit potential (OCP) of Ni-Zn batteries composed of the Zn anode and MoCoCu-P/NF cathodes.

Samples	R_s（Ω cm^2）	R_1（Ω cm^2）
Zn||MoCoCu-P/NF-1	1.634	28.36
Zn||MoCoCu-P/NF-1.5	5.509	13.21
Zn||MoCoCu-P/NF-2	1.187	11.82
Zn||MoCoCu-P/NF-2.5	16.54	8.989

Table S4 Properties of Ni-Zn batteries.

Sample	Capacity (mAh cm^{-2}) (current density mA cm^{-2})	Energy density （mWh cm^{-2}）	Power density （mW cm^{-2}）	Ref.
SiC-Zn‖MoCoCu-P/NF-2	2.82 (40)	4.41	60.2	This work
SiC-Zn‖MoCoCu-P/NF-2	4.0 (15)	6.25	30.1	This work
Zn‖MoCoCu-P/NF-2	2.02 (15)	3.232	24.39	This work
H-$NiMn_xOy$	0.66 (4)	3.34	1.13	[1]
CNSOH-1	2.45 (5)	4.29	52.5	[2]
SANF	0.795 (8)	0.754	69.5	[3]
A-Ni/NC	0.381 (6)	0.035	28	[4]
MNS	1.42 (15)	2.38	99	[5]
ZCNS/NF	2.3 (12)	1.8	36.8	[6]
Zn-Co_3O_4 NWAs/CNTF	1.47 (1)	1.8	36.8	[7]
Cu（$OH)_2$@NiCo-OH	1.12 (3)	1.53	31.6	[8]
Ni-MOF/CNTF	0.4 (0.5)	0.71	8.6	[9]
$NiCo_2O_4$@$CoMoO_4$@Co_3O_4	2.51 (2)	4.09	3.27	[10]

References

[1] Liang X, Zou X, Ren X, et al. Ultrathin nickel manganese nanosheets with rich oxygen-vacancy as a durability electrode for aqueous Ni//Zn batteries. Journal of Colloid and Interface Science, 2020, 578: 677-684.

[2] He W, Wang S, Shao Y, et al. Water invoking interface corrosion: an energy density booster for Ni//Zn battery. Advanced Energy Materials, 2021, 11(9): 2003268.

[3] Wang R, Han Y, Wang Z, et al. Nickel@nickel oxide core-shell electrode with significantly boosted reactivity for ultrahigh-energy and stable aqueous Ni-Zn battery. Advanced Functional Materials, 2018, 28(29): 1802157.

[4] Meng L, Lin D, Wang J, et al. Electrochemically activated nickel-carbon composite as ultrastable cathodes for rechargeable nickel-zinc batteries. ACS Applied Materials & Interfaces, 2019, 11(16): 14854-14861.

[5] Deng Y, Tong X, Pang N, et al. 3D MoS_2/Ni_3S_2 heterogeneous nanorod arrays as high-performance cathode for quasi-solid-state alkaline zinc batteries. Applied Surface Science, 2022, 572: 151442.

[6] Zhou Y, Tong X, Pang N, et al. Ni_3S_2 nanocomposite structures doped with Zn and Co as long-lifetime, high-energy-density, and binder-free cathodes in flexible aqueous nickel-zinc batteries. ACS Applied Materials & Interfaces, 2021, 13(29): 34292-34300.

[7] Li Q, Zhang Q, Zhou Z, et al. Boosting Zn-ion storage capability of self-standing Zn-doped Co_3O_4 nanowire array as advanced cathodes for high-performance

wearable aqueous rechargeable Co//Zn batteries. Nano Research, 2021, 14(1): 91-99.

[8] Shi W, Lian J. Fluffy intersected NiCo-OH nanosheet decorated hollow $Cu(OH)_2$ nanotube arrays on Cu foam for high-performance Ni-Zn battery. Journal of Solid State Chemistry, 2020, 290: 121569.

[9] Li C, Zhang Q, Li T, et al. Nickel metal-organic framework nanosheets as novel binder-free cathode for advanced fibrous aqueous rechargeable Ni-Zn battery. Journal of Materials Chemistry A, 2020, 8(6): 3262-3269.

[10] Xie Y, Fei B, Cai D, et al. Multicomponent hierarchical $NiCo_2O_4$@$CoMoO_4$@ Co_3O_4 arrayed structures for high areal energy density aqueous NiCo//Zn batteries. Energy Storage Materials, 2020, 31: 27-35.

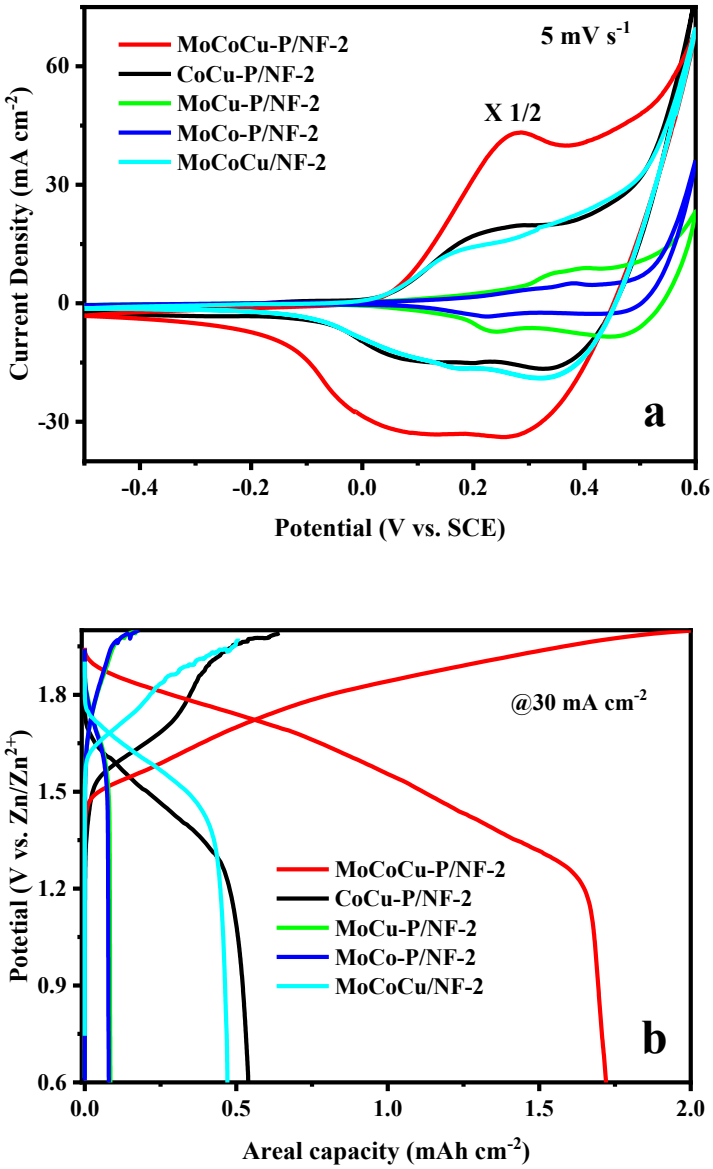

Figure S11 (a) CV curves in 1 mol L^{-1} KOH solution at a scanning rate of 5 mV s^{-1}. (b) Charge-discharge curves of Ni-Zn batteries fabricated with different cathodes (Zn anode).

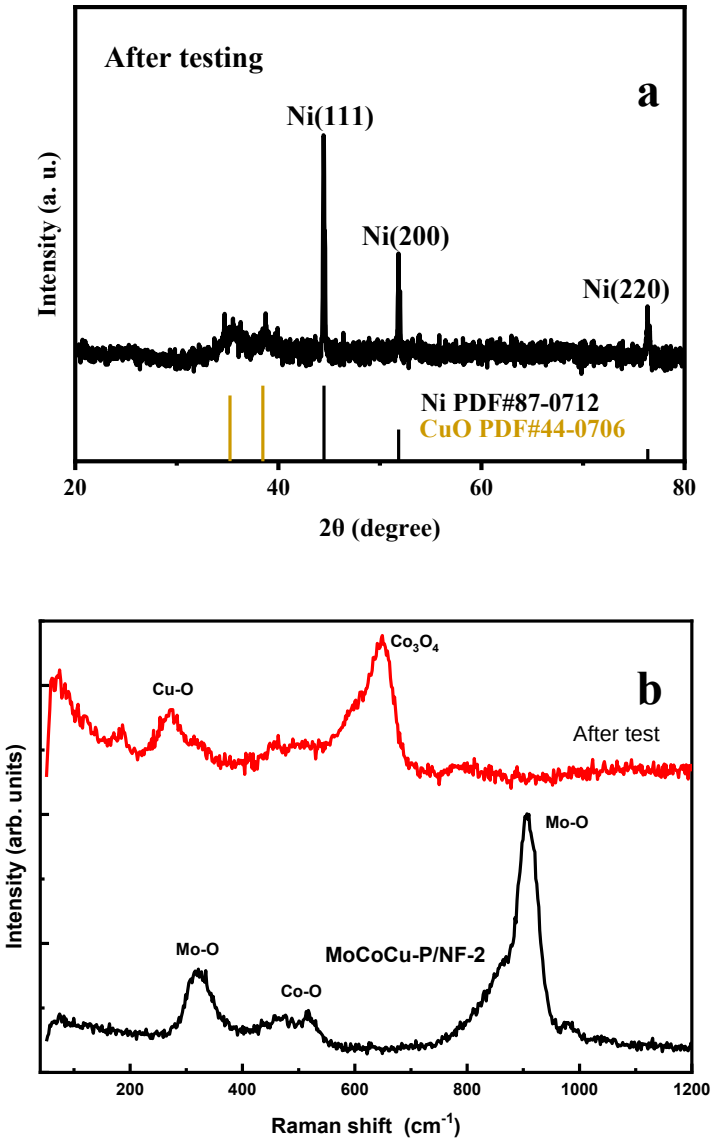

Figure S12 Properties of MoCoCu-P/NF-2 cathode after testing. (a) XRD pattern, (b) Raman spectra.